ACS APPLIED MATERIALS & INTERFACES

www.acsami.org

Research Article

Structural Engineering of the Barrier Oxide Layer of Nanoporous Anodic Alumina for Iontronic Sensing

Juan Wang, Cheryl Suwen Law,* Satyathiran Gunenthiran, Huong Nguyen Que Tran, Khoa Nhu Tran, Siew Yee Lim, Andrew D. Abell,* and Abel Santos*

Cite This: https://doi.org/10.1021/acsami.2c02369

Read Online

ACCESS | Metrics & More | Article Recommendations | Supporting Information

ABSTRACT: The hemispherical barrier oxide layer (BOL) closing the bottom tips of hexagonally distributed arrays of cylindrical nanochannels in nanoporous anodic alumina (NAA) membranes is structurally engineered by anodizing aluminum substrates in three distinct acid electrolytes at their corresponding self-ordering anodizing potentials. These nanochannels display a characteristic ionic current rectification (ICR) signal between high and low ionic conduction states, which is determined by the thickness and chemical composition of the BOL and the pH of the ionic electrolyte solution. The rectification efficiency of the ionic current associated with the flow of ions across the anodic BOL increases with its thickness, under optimal pH conditions. The inner surface of the nanopores in NAA membranes was chemically modified with thiol-terminated functional molecules. The resultant NAA-based iontronic system provides a model platform to selectively detect gold metal ions (Au^{3+}) by harnessing dynamic ICR signal shifts as the core sensing principle. The sensitivity of the system is proportional to the thickness of the barrier oxide layer, where NAA membranes produced in phosphoric acid at 195 V with a BOL thickness of 232 ± 6 nm achieve the highest sensitivity and low limit of detection in the sub-picomolar range. This study provides exciting opportunities to engineer NAA structures with tailorable ICR signals for specific applications across iontronic sensing and other nanofluidic disciplines.

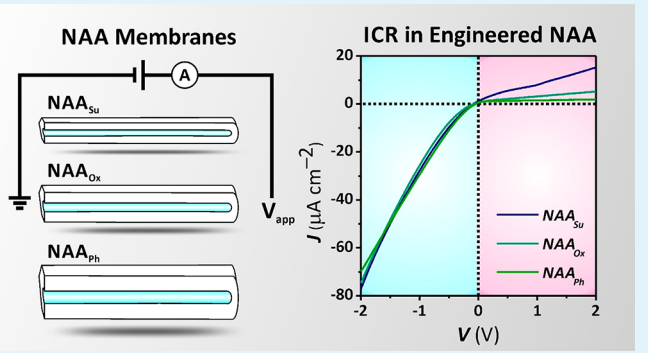

KEYWORDS: *nanoporous anodic alumina, barrier oxide layer, structural engineering, ionic current rectification, surface chemistry, iontronic sensing*

1. INTRODUCTION

Nanoporous anodic alumina (NAA) produced by anodization of aluminum is a versatile nanomaterial with broad trans-disciplinary applicability due to its unique chemical and physical properties and tailorable nanoporous structure.[1−3] NAA is a matrix of anodic aluminum oxide (alumina, Al_2O_3) with arrays of straight, cylindrical, nanometric pores homogeneously distributed across its surface in a honeycomb fashion.[4] This characteristic self-organized porous structure results from an electric field-driven mechano-electrochemical growth mechanism. During the initial stages of the anodization process, nanopores nucleate and grow from top to bottom, perpendicular to the underlying aluminum substrate. The bottom side of each nanopore in the anodic film is closed by a hemispherical layer of anodic oxide—the so-called "barrier oxide layer" or BOL.[5] The BOL provides the growth front of the anodic film, across which two main reactions occur: (i) formation of anodic oxide through electric field-induced oxidation of aluminum by inwardly migrated O^{2-} and OH^- ions at the BOL's metal−oxide interface and (ii) electric field-enhanced dissolution of anodic oxide at the BOL's oxide−electrolyte interface.[6] These reactions are accompanied by a concomitant volume expansion of the anodic oxide over its metal which, under specific conditions, guides nanopores to self-organize in a close-packed hexagonal lattice to minimize mechanical stress localized at the metal−oxide interface between neighboring nanopores.[7] The chemical composition of NAA's nanopores consists of dielectric anodic oxide with an onion-like distribution of ionic impurities and vacancies from the outer to the inner side of the pore wall and the BOL (i.e., oxide−electrolyte and metal−oxide interfaces, respectively).[8] This chemical structure is characterized by two types of ionic defects: (i) acid anion impurities incorporated into the anodic oxide from the electrolyte, the concentration of which decreases from the outer (contaminated Al_2O_3) to the inner

Received: February 8, 2022
Accepted: April 14, 2022

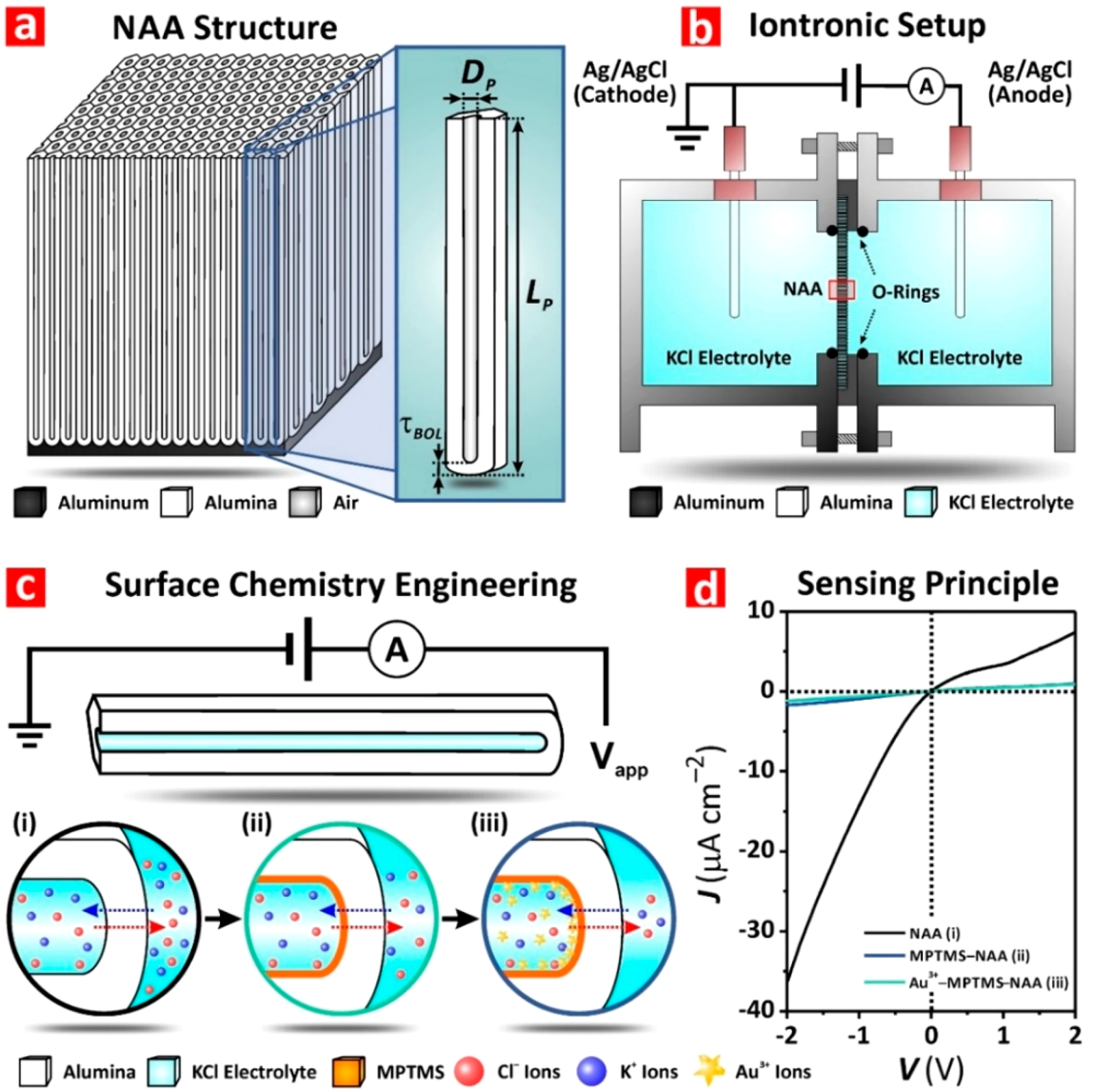

Figure 1. Engineering of the barrier oxide layer (BOL) of nanoporous anodic alumina (NAA) for iontronic sensing. (a) Schematic depicting the structure of NAA membranes with a BOL, with the definition of the main geometric features (i.e., nanopore diameter, D_P; nanopore length, L_P; and BOL thickness, τ_{BOL}). (b) Schematic illustrating the iontronic setup (H-cell) used to measure the current density–voltage (J–V) characteristic of NAA-based iontronic systems, in which NAA membranes are placed between two half-cells containing KCl electrolyte and a potential between two Ag/AgCl electrodes is applied (NB: NAA's BOL outer side facing the anode (V_{app}) and NAA's BOL inner side facing the cathode (ground)). (c) Illustration of the nanopore–electrode system configuration and the three sensing stages with flow of K^+ and Cl^- ions across the NAA's BOL in (i) as-produced NAA, (ii) (3-mercaptopropyl)trimethoxysilane (MPTMS)-functionalized NAA, and (iii) MPTMS–NAA after selective binding of Au^{3+} ions. (d) J–V profiles associated with stages (i), (ii), and (iii) shown in part c, with dynamic shifts in the characteristic ICR signal (NB: NAA membrane produced in sulfuric acid electrolyte).

(pure Al_2O_3) side of the pore wall and the BOL, and (ii) negative (O^{2-}) and positive (Al^{3+}) defect charge vacancies distributed across the volume of the amorphous BOL, where the number of O^{2-} vacancies is higher than that of the stoichiometric ratio for Al_2O_3 (i.e., 1.5) at the oxide–electrolyte interface.[9−13] Ionic impurities and charge vacancies result from the flow of electrolytic species (i.e., O^{2-}, HO^-, Al^{3+}, COO^-, SO_4^{2-}, and PO_4^{3-}) across the BOL during the electric field-assisted growth of anodic oxide under volume expansion and compressive stress.[14] The unique structure of NAA with well-defined nanopores provides an ideal material to develop membranes with precisely engineered properties for nanofluidic and separation applications.[15,16] Of all these, NAA structures have recently been devised as model platforms for nanopore-based iontronics—generation and transmission of electric signals associated with the flow of ions along bioinspired, synthetic nanochannels.[17] Pioneering NAA-based iontronic systems were based on through-hole membranes, in which the BOL was selectively removed to create arrays of cylindrical nanopores connecting the two reservoirs of an H-cell containing an equal concentration of potassium chloride (KCl) electrolyte.[18−21] Generation of asymmetry in surface charge and/or geometry along the nanopore length in these NAA membranes was demonstrated to selectively allow or forbid the flow of either cations or anions under an electric field bias applied between the two electrodes at each reservoir of the H-cell.[22] Since electrolytes are ionic conductors but electronic insulators, the electric field-driven motion of ions

https://doi.org/10.1021/acsami.2c02369
ACS Appl. Mater. Interfaces XXXX, XXX, XXX−XXX

through the engineered nanopores of NAA results in the accumulation of space charges at the electrolyte−nanopore wall interface to form an electric double layer (EDL).[23] The EDL acts as a parallel plate capacitor, which overlaps with the nanopore walls so mobile counterions (i.e., cations or anions) compensate surface charges to maintain charge neutrality. As such, ionic flow along the nanopores of through-hole NAA membranes enables functions that resemble those of solid-state diodes and transistors such as rectification and switching by harnessing synaptic-like, ion-based signal transduction mechanisms.[24] Advances in iontronics systems have successfully realized various forms of biomimetic functions such as molecular and chemical logic gates,[25] microelectrochemical logic circuits,[26] DNA computing,[27] ion pumps,[28] energy generation,[29] and sensing.[30] These systems integrate distinct passive or active chemical and physical stimuli to control ionic flow such as nanopore structure,[31] voltage,[32] pH,[33] light,[21] chemical composition,[34] temperature,[35] and pressure.[36] However, recent studies[13,37] reveal that the BOL in blind-hole NAA membranes has an intrinsic characteristic ionic current rectification (ICR) signal between high and low conduction states, which has been associated with the flow of ions across a hybrid structure of nanopores and ionic nanochannels (i.e., 0.0−1.3 nm) in the anodic BOL. This unique property provides a core sensing principle to develop a range of iontronic sensors for distinct types of analytes (e.g., proteins, cells, microRNA, and metal ions).[37−40] A recent milestone study by Kim and co-workers has provided a mechanistic model that describes the intriguing ICR properties of NAA's BOL. In this model, the characteristic ICR signal of NAA's BOL is attributed to the space charge density gradient of the O^{2-} and Al^{3+} charge vacancies distributed across its volume.[13] As such, since the generation and distribution of space charge vacancies across the BOL rely intrinsically on the electric field-driven flow of electrolytic species during the growth of anodic oxide,[13] we hypothesize that it should be possible to engineer ICR signals in blind-hole NAA structures through anodization. Here we engineer the structure of NAA's BOL by anodizing aluminum in sulfuric, oxalic, and phosphoric acid electrolytes at their corresponding self-ordering anodizing potentials (Figure 1a). The BOL of these NAA structures features a characteristic ICR signal that depends on the thickness and chemical composition of the anodic oxide and the pH of the ionic electrolyte solution, where the ICR ratio increases with the thickness of the BOL at optimal pH (Figure 1b). The inner surface of nanopores in NAA membranes is then functionalized with thiol-terminated functional molecules to create a model iontronic system to selectively detect gold metal ions (Au^{3+}) (Figure 1c). Dynamic shifts in the BOL's ICR signal associated with binding of Au^{3+} ions to thiol functional groups on the inner surface of blind-hole NAA membranes provide a transduction principle to elucidate the dependence of ICR sensitivity on the characteristics of the anodic BOL (Figure 1d). Our findings indicate that the sensitivity of the system can be enhanced by engineering the characteristic BOL of NAA, where the thicker the BOL, the more sensitive the iontronic system is.

2. EXPERIMENTAL SECTION

2.1. Materials. 99.9997% pure aluminum (Al) sheets with a nominal thickness of 320 μm were supplied by Goodfellow Cambridge Ltd. (UK). Perchloric acid ($HClO_4$), copper(II) chloride ($CuCl_2$), oxalic acid ($C_2H_2O_4$), chromium trioxide (CrO_3), chloroauric acid ($HAuCl_4$), and (3-mercaptopropyl)trimethoxysilane (MPTMS, $HS(CH_2)_3Si(OCH_3)_3$) were purchased from Sigma-Aldrich (Australia). Hydrochloric acid (HCl), ethanol (EtOH, C_2H_5OH), potassium chloride (KCl), potassium hydroxide (KOH), hydrogen peroxide (H_2O_2), nitric acid (HNO_3), phosphoric acid (H_3PO_4), and sulfuric acid (H_2SO_4) were provided by ChemSupply (Australia). Milli-Q water (18.2 MΩ cm) was used to prepare all aqueous solutions.

2.2. Fabrication of NAA Membranes. As-received Al sheets were cut into 1.5 × 1.5 cm^2 square chips and then sequentially washed in ethanol and Milli-Q water under sonication for 5 min each to remove impurities from the surface. Clean Al chips were air-dried and stored under dry atmosphere. To avoid undesired effects associated with localized electric field and the enable homogeneous, self-organized pore growth, Al chips were electropolished in an electrolyte mixture containing 4:1 (v:v) EtOH:$HClO_4$ to smooth their surface roughness. This process was performed at an electrolyte temperature of ∼5 °C and a potential of 20 V for 3 min under continuous, vigorous stirring. To engineer the geometric features of the BOL in NAA membranes, electropolished Al substrates with a mirror-like finish were anodized by the two-step process in three distinct water-based acid electrolytes at their corresponding self-organization potentials and temperatures (i.e., 0.3 M sulfuric acid at 25 V and 6 °C, 0.3 M oxalic acid at 40 V and 6 °C, and 0.1 M phosphoric acid at 195 V at −2 °C).[41−44] Details of the anodization conditions used in these two-step processes are summarized in Table 1. The duration of the second anodization step was adjusted accordingly to obtain a nominal thickness of ∼43 μm in all NAA membranes. After anodization, Al substrate remaining at the backside of NAA membranes was selectively removed by wet chemical etching in a mixture solution of HCl (2.4 M) and $CuCl_2$ (0.2 M) to expose the BOL at the bottom side. This etching process was performed in a PVC-based etching cell through a 0.4-cm-diameter rubber O-ring as the etching mask. Upon complete removal of the aluminum substrate, a drop of HNO_3 was poured on the bottom side of the NAA membrane for a couple of seconds to remove any copper/aluminum residue. This step was followed by a thorough washing in Milli-Q water, after which NAA membranes were air-dried. Next, Al substrate remaining at the top and backside was masked by a layer of nail polish and cured at 45 °C to electrically insulate the NAA membrane from the metal and avoid potential parasite current interferences that could alter iontronic signals associated with the flow of ions across the BOL. The average area of the unmasked region of these NAA membranes estimated by image analysis was determined to be ∼0.12 cm^2 (Figure S1, Supporting Information).

Table 1. Fabrication Conditions Used to Produce Nanoporous Anodic Alumina (NAA) Membranes in Sulfuric, Oxalic, and Phosphoric Acid Electrolytes (NAA_{Su}, NAA_{Ox}, and NAA_{Ph}) under Their Corresponding Self-organization Regimes through the Two-Step Anodization Process[a]

NAA	Acid Electrolyte	Concentration (M)	T (°C)	V (V)	t (h)
NAA_{Su}	Sulfuric (H_2SO_4)	0.3	6	25	8[b]
NAA_{Ox}	Oxalic ($H_2C_2O_4$)	0.3	6	40	16[b]
NAA_{Ph}	Phosphoric (H_3PO_4)	0.1 (10% v EtOH)[d]	−2	195	27[c]

[a]NB: electrolyte temperature, T; second step anodization time, t. [b]The first anodization step for NAA_{Su} and NAA_{Ox} membranes was performed for 24 h. [c]The first anodization step for NAA_{Ph} was performed in three stages: (i) 175 V for 4 h, (ii) increment of anodizing voltage at a rate of 0.0025 V s^{-1} to 195 V and (iii) 195 V for 27 h. [d]The aqueous H_3PO_4 acid electrolyte was modified with EtOH to prevent it from freezing at subzero temperatures.

https://doi.org/10.1021/acsami.2c02369
ACS Appl. Mater. Interfaces XXXX, XXX, XXX−XXX

2.3. Iontronic Characterization of NAA Membranes. A custom-designed, Teflon H-cell was used to characterize iontronic current density−voltage (J−V) profiles of NAA membranes. In this system, NAA membranes were sandwiched between the two half-cells of the H-cell via Viton O-rings with a diameter of 1 cm. Once sealed, the half-cells were simultaneously filled with 0.1 M KCl solutions, the pH of which was adjusted to the specific value with dropwise addition of aqueous 0.1 M HCl and 0.1 M KOH. The pH of the solution was measured in real time with a calibrated pH meter at room temperature (i.e., ∼25 °C). The J−V characteristic of NAA membranes was analyzed by applying a potential (V_{app}) from the anode (inner side of the BOL) to the cathode/ground (outer side of the BOL) using two single junction silver chloride (Ag/AgCl, saturated KCl) reference electrodes (model RREF0021 Pine Research Instrumentation, USA). Iontronic J−V profiles were acquired by scanning V_{app} from −2 to +2 V at a rate of 0.1 V s^{-1} using a biopotentiostat (CHI 760E, CHI Instruments Inc., USA). All iontronic measurements were performed at room temperature throughout within a customized Faraday cage under dark conditions to prevent electromagnetic interferences (Figure S1, Supporting Information). The BOL of NAA membranes was also characterized in the same electrochemical setup via electrochemical impedance spectroscopy (EIS). The frequency of an input sinusoidal AC voltage of 0.05 V was varied from 1×10^{-2} to 1×10^{6} Hz at the fixed DC potentials of −2, 0, and 2 V. The equivalent circuit was determined from the obtained Nyquist impedance spectra, using an in-built IMP application in the biopotentiostat.

2.4. Chemical Functionalization of NAA Membranes. The inner surface (i.e., outer side of the BOL) of a set of freshly prepared NAA membranes produced in sulfuric, oxalic, and phosphoric acid electrolytes (i.e., NAA_{Su}, NAA_{Ox}, and NAA_{Ph}) was chemically functionalized with MPTMS via wet phase deposition. Note that as-produced NAA membranes were selectively functionalized from the top side before removing the backside Al substrate to prevent the outer side of the BOL from functionalization. In this process, as-produced NAA membranes were first hydroxylated by immersion in H_2O_2 (35 wt%) at 100 °C for 10 min to increase the number of hydroxyl groups (-OH) on the surface of anodic Al_2O_3. After this, hydroxylated NAA membranes were dipped into an EtOH-based solution containing 1 mM MPTMS under a sealed atmosphere and continuous, slight stirring for 3 h to favor the formation of self-assembled MPTMS monolayers. Then, MPTMS-modified NAA membranes were washed thoroughly with EtOH to remove unbound MPTMS molecules, dried under air stream, and annealed at 110 °C for 1 h in an oven to stabilize and cross-link the thiol-containing silane functional layer on the inner surface of the NAA membranes.

2.5. Water Contact Angle and Isoelectric Point Measurements. The water contact angle of as-produced and MPTMS-functionalized NAA membranes was characterized by an optical tensiometer using the sessile drop technique (Attention Theta Flex, Biolin Scientific, Sweden). In this system, a water droplet with an average volume of ∼15 μL was formed on the tip of a syringe needle. After this, the end of the needled was brought near the top surface of NAA membranes until contact and automatically retracted. Upon stabilization, contact angles at both sides of the water droplet on the surface of NAA membranes were determined through image analysis, using a custom-built application. The zeta potential of NAA membranes was determined from suspended particles of NAA in 1 mL of 0.01 M KCl solution, the pH of which was varied from 3 to 10. NAA suspensions with controlled pH were then transferred into a zeta cell, and the respective zeta potential was measured at 25 °C after an equilibration time of 30 s, using a ZetaSizer Nano (Malvern Instruments Ltd., Malvern Panalytical, UK). The average values of the refractive index and absorption coefficient of anodic Al_2O_3 were assumed to be 1.76 and 0.01, respectively.[45]

2.6. Structural Characterization of NAA Membranes. The geometric features of NAA membranes (i.e., nanopore diameter D_P, interpore distance D_{Int}, nanopore length L_P, and barrier oxide layer thickness τ_{BOL}) were characterized by analyzing field emission gun scanning electron microscopy images (FEG-SEM Quanta 450, FEI, USA) in ImageJ software.[46]

3. RESULTS AND DISCUSSION

3.1. Electrochemical Engineering of NAA Membranes. Figure 2 shows a schematic describing the two-step anodization process used to engineer NAA membranes. This process is performed in an electrochemical reactor equipped with temperature control and continuous stirring to facilitate the diffusion of ionic species involved in the formation and dissolution of alumina from the bulk electrolyte to the BOL at the nanopore bottom tips (Figure 2a).

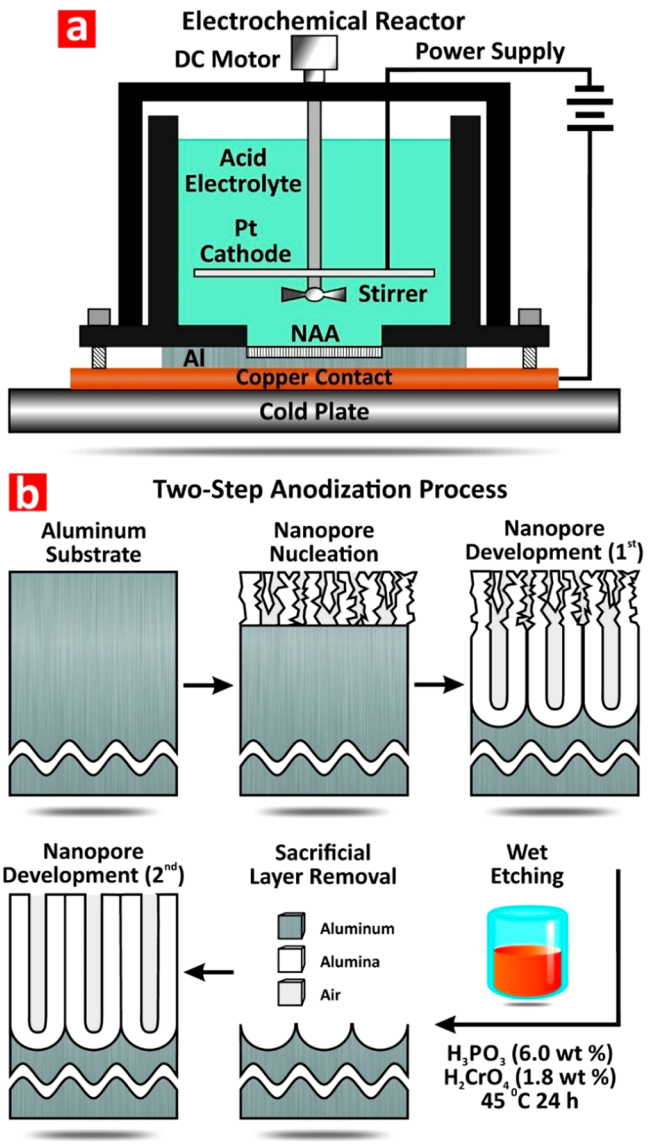

Figure 2. Electrochemical fabrication of NAA membranes by the two-step anodization process. (a) Schematic showing the structure of the electrochemical reactor used to anodize aluminum under stirring and controlled temperature conditions. (b) Fabrication diagram depicting the two-step anodization process with electropolished aluminum substrate, nanopore nucleation in an anodic film (initial stage of the first anodization step), nanopore growth, chemical wet etching to remove a sacrificial anodic layer, and a second anodization step.

After electropolishing, Al substrates are anodized in acid electrolytes at their corresponding anodizing potential (Figure 2b and Table 1). During the first stages of the anodization process, nanopores nucleate across the surface of the anodic oxide film and grow in depth. Under specific conditions, the

https://doi.org/10.1021/acsami.2c02369
ACS Appl. Mater. Interfaces XXXX, XXX, XXX−XXX

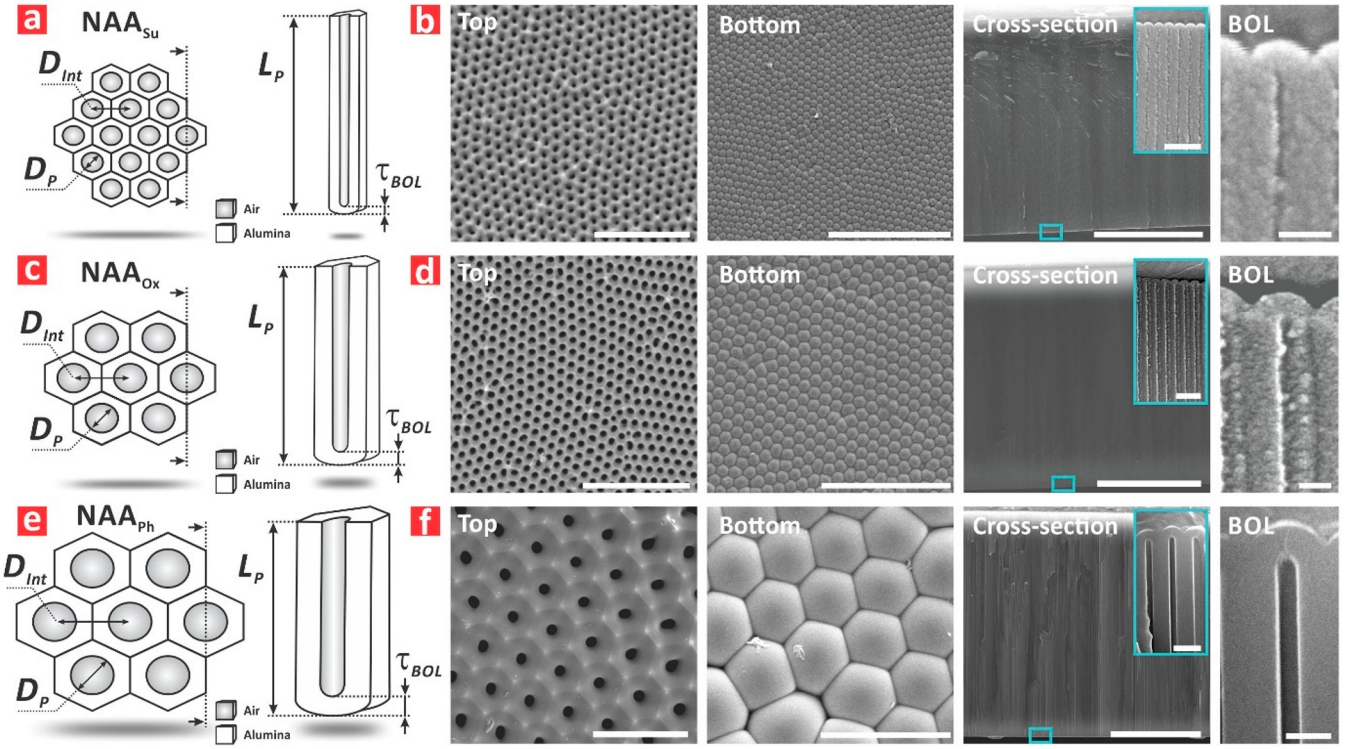

Figure 3. Structural characterization of the main geometric features (D_P, D_{Int}, L_P, and τ_{BOL}) of NAA membranes produced by the two-step anodization process. (a) Schematics describing the main geometric features of NAA_{Su} membranes. (b) Top view (first column), bottom view (second column), general and magnified cross-sectional view (third column and inset), and BOL view (fourth column) FEG-SEM images of NAA_{Su} membranes (NB: scale bars from left to right: 500 nm, 1 μm, 20 μm, 200 nm, and 50 nm). (c) Schematics describing the main geometric features of NAA_{Ox} membranes. (d) Top view (first column), bottom view (second column), general and magnified cross-sectional view (third column and inset), and BOL view (fourth column) FEG-SEM images of NAA_{Ox} membranes (NB: scale bars from left to right: 1 μm, 1 μm, 20 μm, 250 nm, and 50 nm). (e) Schematics describing the main geometric features of NAA_{Ph} membranes. (f) Top view (first column), bottom view (second column), general and magnified cross-sectional view (third column and inset), and BOL view (fourth column) FEG-SEM images of NAA_{Ph} membranes (NB: scale bars from left to right: 1 μm, 1 μm, 20 μm, 500 nm, and 250 nm).

hemispherical BOL guides the self-organization of nanopores inside the anodic film by minimizing the mechanical stress induced by the anodic oxide-to-metal volume expansion between adjacent nanopores. It is worth noting that a slightly different approach was adapted for anodization of aluminum using phosphoric acid since direct anodization of electropolished aluminum at high voltage (195 V) results in catastrophic burning of the anodic oxide due to increased local Joule heat generated at the pore bottom tips. A preanodization step at lower voltage (175 V) with a slow ramp rate of 0.025 V s^{-1} to reach 195 V makes it possible to avoid catastrophic breakdown of the anodic oxide film.[47] After ~24 h, self-organized nanopores follow a close-packed, honeycomb-like arrangement. But this organized structure is limited to the bottom side of the anodic film, whereas its top side features disordered nanopores. To address this, the sacrificial anodic oxide film resulting from the first anodization step is chemically dissolved in an aqueous mixture of H_3PO_4 and H_2CrO_4 at 45 °C for ~24 h.[48] After removal, the exposed underlying aluminum substrate features a pattern of hemispherical, highly ordered concavities due to the deep texturing of aluminum from a long first anodization step (~24 h), which are a negative replica of the bottom side of the sacrificial NAA film.[49] As such, when a second anodization step is performed under the same conditions as those used during the first step, nanopores nucleate at the center of each concavity across the patterned aluminum substrate (i.e., one nanopore per concavity) because of the localized concentration of the electric field. After nucleation, nanopores propagate perpendicularly to the aluminum substrate with straight coherency, from top to bottom, while maintaining the original hexagonal arrangement. The thickness of the resulting membrane can be judiciously adjusted by either the anodization time or the total charge (i.e., integrated current density over time). In our study, the anodization time of the second step was set to generate NAA_{Su}, NAA_{Ox}, and NAA_{Ph} membranes with a nominal thickness of ~43 μm based on the oxide growth rate in each acid electrolyte: ~5.3 μm h^{-1} for sulfuric acid, ~2.7 μm h^{-1} for oxalic acid, and 1.7 μm h^{-1} for phosphoric acid (Table 1). The structure of NAA is a matrix of alumina featuring arrays of cylindrical, straight nanopores arranged in hexagonal cells, where each nanopore is closed by a hemispherical BOL at its bottom tip (i.e., metal−oxide interface). Structurally, NAA membranes can be defined by four main geometric features: nanopore diameter (D_P), interpore distance (D_{Int}), nanopore length or thickness of the anodic film (L_P), and barrier oxide layer thickness (τ_{BOL}).

Figure 3 shows the schematics and top, bottom, and cross-sectional FEG-SEM images of NAA_{Su}, NAA_{Ox}, and NAA_{Ph} membranes produced by the two-step anodization process under self-organization conditions. The average values of these geometric features estimated via FEG-SEM image analysis were 19 ± 5, 46 ± 5, and 108 ± 13 nm for D_P, 64 ± 5, 110 ± 3, and 490 ± 12 nm for D_{Int}, and 33 ± 4, 53 ± 5, and 232 ± 6

https://doi.org/10.1021/acsami.2c02369
ACS Appl. Mater. Interfaces XXXX, XXX, XXX−XXX

nm for τ_{BOL} for NAA_{Su}, NAA_{Ox}, and NAA_{Ph} membranes, respectively (Table 2). According to the high field conduction theory describing the electric field-driven movement of electrolytic species involved in the formation and dissolution of anodic oxide across the barrier oxide layer of NAA, the thickness of the BOL in the NAA membranes increases proportionally with the anodizing potential at a rate of ~1 nm V^{-1} under mild conditions.[1] The range of BOL thickness covered in our study (i.e., from ~30 to ~230 nm) cannot be achieved with one single acid electrolyte due to the breakdown potential (i.e., anodizing potential above which there is catastrophic flow of current, and consequent burning and cracking of the anodic oxide film). Furthermore, the anodizing potential under which NAA achieves its self-organization regime increases in the order sulfuric < oxalic < phosphoric (i.e., 25 V for 0.3 M sulfuric acid, 40 V for 0.3 M oxalic acid, and 195 V for 0.1 M phosphoric acid). The main objective of our study was to elucidate the effect of the BOL thickness on

Table 2. Geometric Features (D_P, D_{Int}, L_P, and τ_{BOL}) Determined by FEG-SEM Image Analysis Describing the Structure of Nanoporous Anodic Alumina (NAA) Membranes Produced in Sulfuric, Oxalic, and Phosphoric Acid Electrolytes (NAA_{Su}, NAA_{Ox}, and NAA_{Ph}) under Their Corresponding Self-organization Regimes through the Two-Step Anodization Process

NAA	D_P (nm)	D_{Int} (nm)	L_P (μm)	τ_{BOL} (nm)
NAA_{Su}	19 ± 5	64 ± 5	42.7 ± 0.2	33 ± 4
NAA_{Ox}	46 ± 5	110 ± 3	42.6 ± 0.4	53 ± 5
NAA_{Ph}	108 ± 13	490 ± 12	45.1 ± 0.4	232 ± 6

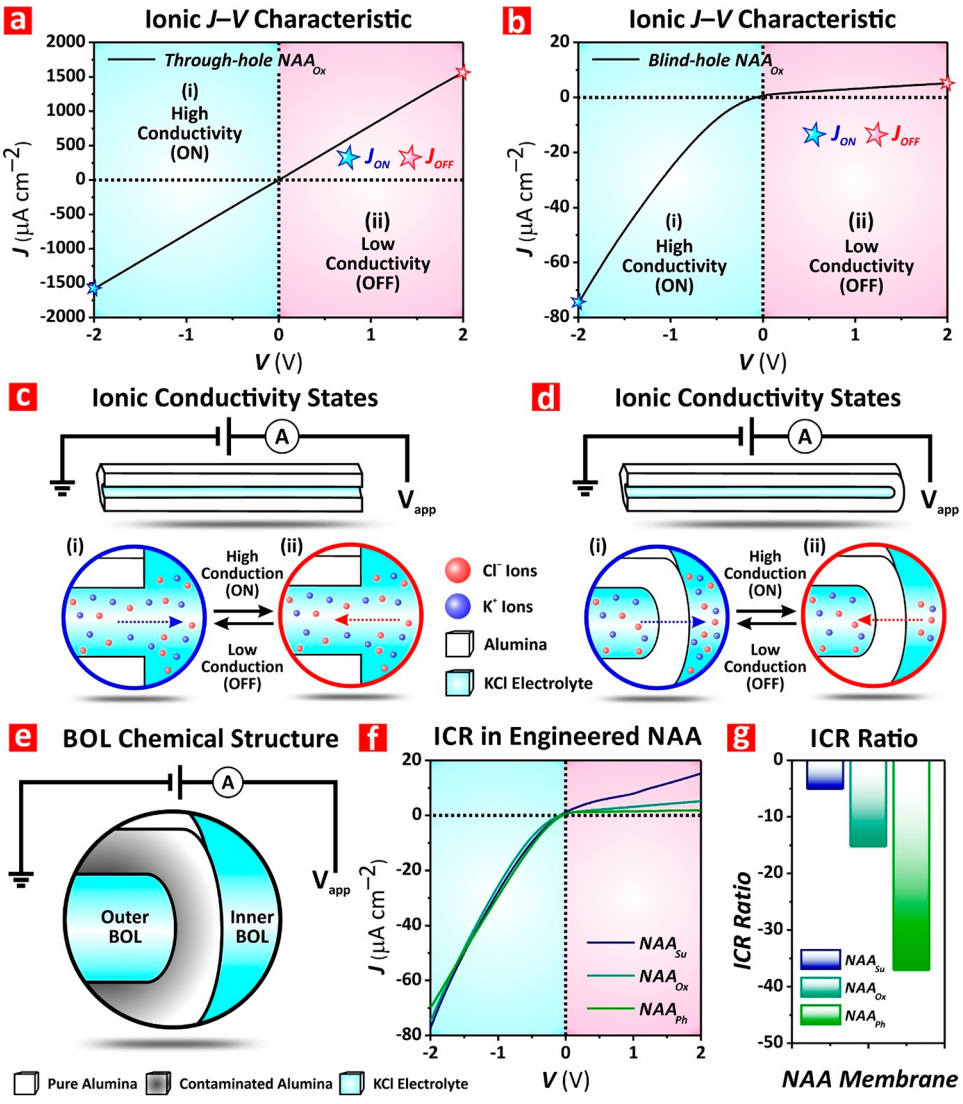

Figure 4. Characterization of ionic current rectification (ICR) in engineered NAA membranes (NB: all blind-hole NAA membranes were subjected to the reset process prior to J–V characterization). (a) Ionic J–V characteristic of a through-hole NAA_{Ox} membrane in 0.1 M KCl at pH = 6. (b) Ionic J–V characteristic of a blind-hole NAA_{Ox} membrane in 0.1 M KCl at pH = 6. (c and d) Schematics describing the flow of K^+ and Cl^- ions under high and low ionic conduction states in through-hole and blind-hole NAA membranes, respectively. (e) Illustration showing the configuration used to measure the J–V characteristic of engineered NAA membranes and the onion-like distribution of impurities and ionic vacancies across their BOL. (f) J–V characteristic of blind-hole NAA_{Su}, NAA_{Ox}, and NAA_{Ph} membranes in 0.1 M KCl under optimal pH conditions (i.e., 6, 6, and 3, respectively). (g) ICR ratio of blind-hole NAA_{Su}, NAA_{Ox}, and NAA_{Ph} membranes in 0.1 M KCl under optimal pH conditions (i.e., 6, 6, and 3, respectively) estimated from part f.

https://doi.org/10.1021/acsami.2c02369
ACS Appl. Mater. Interfaces XXXX, XXX, XXX–XXX

the ionic rectification efficiency across the BOL of self-organized NAA membranes produced under mild anodization conditions. To this end, the BOL thickness must be varied over a wide range of values, which requires the use of distinct acid electrolytes and justifies our selection.

3.2. Ionic Current Rectification Characterization of NAA Membranes. Parts a and b of Figure 4 summarize the ionic current density−voltage (J−V) characteristic of two representative NAA membranes produced in oxalic acid electrolyte with a through-hole (without BOL) and blind-hole (with BOL) structure in a 0.1 M KCl electrolyte at pH 6, respectively. The former type of NAA membrane featuring symmetric straight cylindrical nanopores with both ends open and constant surface charge density displays a characteristically linear J−V behavior, in which the absolute values of J at the ON and OFF states are equal ($|J_{ON}| = |J_{OFF}|$, Figure 4a).[50] In contrast, ionic conduction across the blind-hole NAA membrane with a barrier oxide layer at the bottom of its nanopores shows a nonlinear J−V characteristic. This profile resembles that of an electronic diode with high (ON) and low (OFF) ionic conduction states at $V_{app} < 0$ V and $V_{app} > 0$ V, respectively, where $|J_{ON}| > |J_{OFF}|$ (Figure 4b). Upon application of positive ($V_{app} > 0$ V) and negative ($V_{app} < 0$ V) bias, K^+ and Cl^- ions can flow freely along the nanopores of through-hole NAA membranes from one half-cell of the H-cell to the other, since both nanopore diameter and surface charge density are constant. As such, the ionic currents associated with the flow of ions at the ON and OFF states are equal ($|J_{ON}| = |J_{OFF}|$, Figure 4c). However, while the flow of K^+ and Cl^- ions under a positive bias ($V_{app} > 0$ V) in blind-hole NAA membranes is forbidden, there is some flow of ions across the BOL under a negative bias ($V_{app} < 0$ V) (Figure 4d). This ionic current rectification (ICR) characteristic has been attributed to the distribution of space charge density associated with positive (Al^{3+}) and negative (O^{2-}) defect vacancies across the BOL's volume. The growth of NAA involves the formation and dissolution of oxide at the barrier oxide layer (BOL) under dynamic equilibrium conditions (i.e., the rates of formation and dissolution of oxide are balanced). At the oxide−electrolyte interface, O^{2-} ions are generated from the heterolytic dissociation of water molecules. Simultaneously, Al^{3+} ions are both released into the electrolyte from the dissolution of alumina at the oxide−electrolyte interface and ejected from the Al substrate into the oxide to undergo oxidation by O^{2-} ions and form anodic oxide at the metal−oxide interface. Under high electric field, the counter migration of oppositely charged ions occurs via hopping from vacancies to vacancies, which in turn redistributes the ionic defect species in the BOL. These vacancies or point defects are made up of aluminum and oxygen vacancies, which are generated during anodization and represent fixed space charges, and their distribution in the BOL forms a gradient along the direction from the metal−oxide to oxide−electrolyte interfaces.[14] Since all NAA membranes assessed in our study were produced under the mild anodization regime, it is reasonable to infer that the space charge density gradient in NAA membranes will be influenced by the thicknesses of their BOLs (Figure 4e). Therefore, we hypothesize that this ICR characteristic should be different in NAA membranes produced in distinct electrolytes under their corresponding self-ordering anodization conditions. Indeed, analysis of the ICR characteristic of NAA_{Su}, NAA_{Ox}, and NAA_{Ph} membranes at their optimal pH in 0.1 M KCl (i.e., pH at which the ICR ratio is maximum) reveals that, whereas the current density at the ON state (J_{ON}) is comparable (i.e., average value of $J_{ON} = -74 \pm 4$ mA cm^{-2}), the ionic conduction at the OFF state in these blind-hole membranes relies on the type of NAA membrane, with estimated values of $J_{OFF} = 15.2 \pm 3.1$, 5.1 ± 1.0, and 0.3 ± 0.1 mA cm^{-2}, respectively (Figure 4f). Analysis of the ICR ratio, defined by $|J_{ON}/J_{OFF}|$ at $|V_{app}| = 2$ V, shows that rectification in blind-hole NAA membranes increases in the order $NAA_{Su} < NAA_{Ox} < NAA_{Ph}$ at optimal pH conditions, with values of −5, −15, and −37, respectively (Figure 4g). Note that in this context, a negative ICR ratio denotes that the ON state occurs under negative bias ($V_{app} = -2$ V), whereas a positive ICR ratio indicates that the high ionic conduction state takes place under positive bias ($V_{app} = 2$ V). Therefore, blind-hole NAA membranes achieve the highest ionic rectification performance under a negative bias at their corresponding optimal pH, and their ICR efficiency increases with the BOL thickness.

It is worthwhile to note that ionic rectification in as-produced NAA membranes is not stable and changes with the number of measured J−V cycles. To address this drawback, Kim and co-workers devised the so-called "reset process", in which cyclic voltage sweeps are applied across NAA membranes in ultrapure water until stabilization of their J−V characteristic. Application of this process to NAA membranes produced in sulfuric, oxalic, and phosphoric acid reveals a similar trend to that reported by Kim and co-workers in their study on NAA_{Ox} membranes. Figure S2 (Supporting Information) summarizes the obtained results, in which it is apparent that the current density at the ON and OFF states (i.e., $|V_{app}| = 2$ V) changes with voltage sweeps until it gradually reaches a steady state after 21 voltage cycles. However, NAA_{Su}, NAA_{Ox}, and NAA_{Ph} membranes show interesting differences. For instance, the absolute values of J_{ON} and J_{OFF} are found to decrease with increasing thickness of the BOL, whereas the value of J_{ON} for NAA_{Su} is approximately 1 order of magnitude larger than that of the NAA_{Ph} counterpart. It is also observed that the ON reset state of NAA membranes produced in sulfuric acid occurs under a negative potential bias ($V_{app} < 0$ V), whereas the ON state for NAA_{Ox} and NAA_{Ph} membranes during the reset process is at $V_{app} > 0$ V. This analysis also indicates that NAA_{Ph} membranes provide more stable J−V signals under continuous voltage cycles than their NAA_{Ox} and NAA_{Su} analogs. To gain further insights into the iontronic characteristics of the BOL of blind-hole NAA membranes produced in sulfuric, oxalic, and phosphoric acid, we performed electrochemical impedance spectroscopy (EIS) analysis in 0.1 M KCl electrolyte after the reset process. Figure S3 (Supporting Information) summarizes the Nyquist spectra of NAA_{Su}, NAA_{Ox}, and NAA_{Ph} membranes at $V_{app} = -2$, 0, and 2 V, along with details of the equivalent circuit model developed by Kim and co-workers used to estimate the values of the resistance of their BOL (R_{BOL}) in 0.1 M KCl at their optimal pH (eqs S1 and S2 and Table S1 in Supporting Information).[13] Analysis of the values summarized in Table 3 indicates that R_{BOL} increases when the system transitions from its ON ($V_{app} = -2$ V) to its OFF ($V_{app} = -2$ V) state. Interestingly, this result indicates that NAA_{Su}, NAA_{Ox}, and NAA_{Ph} membranes have similar values of R_{BOL} at $V_{app} = -2$ V (ON state) with an average of 0.7 ± 0.3 kΩ·cm^2, whereas the value of R_{BOL} at $V_{app} = 2$ V (OFF state) increases with the thickness of the BOL, with values of 2.8, 4.5, and 8.3 kΩ·cm^2, respectively. This result is in good agreement with our observations of ICR characteristics in these membranes

https://doi.org/10.1021/acsami.2c02369
ACS Appl. Mater. Interfaces XXXX, XXX, XXX−XXX

Table 3. Values of the Resistance of the BOL of NAA Membranes Produced in Sulfuric, Oxalic, and Phosphoric Acid Electrolytes (NAA_{Su}, NAA_{Ox}, and NAA_{Ph}) Estimated by EIS in 0.1 M KCl at Their Optimal pH

	R_{BOL} (kΩ·cm^2)		
NAA	V_{app} = −2 V	V_{app} = 0 V	V_{app} = 2 V
NAA_{Su}	0.6	1.8	2.8
NAA_{Ox}	1.0	1.8	4.5
NAA_{Ph}	0.5	1.2	8.3

(Figure 4f), where the current density at J_{OFF} decreases in the order NAA_{Su} > NAA_{Ox} > NAA_{Ph}.

3.3. pH-Dependent Ionic Current Rectification in Engineered NAA Membranes. Figure 5 shows the dependence of the $J-V$ characteristic of blind-hole NAA_{Su}, NAA_{Ox}, and NAA_{Ph} membranes in a 0.1 M KCl electrolyte at varying pH values, from 3 to 10. These graphs indicate that the high ionic conduction state (J_{ON}) occurs under a negative bias (V_{app} = −2 V) from pH 3 to 9 for all NAA membranes. However, the polarity of the system is reversed for pH > 9, where the J_{ON} state occurs under a positive bias (V_{app} = 2 V). This result is in good agreement with the observations reported by Kim and colleagues using NAA_{Ox} membranes produced under similar anodization conditions.[13] To gain further insight into this intriguing characteristic, we analyzed the dependence of the isoelectric point (IEP) and ICR ratio of these model systems. The IEP is defined by the pH value at which the surface charge density of NAA (σ_{S-NAA}) becomes zero (i.e., pH turning point between σ_{S-NAA} > 0 C·m^{-2} and σ_{S-NAA} < 0 C·m^{-2}). NAA is known to be positively charged ($Al-OH_2^+$) at pH < IEP_{NAA} and negatively charged ($Al-O^-$) at pH > IEP_{NAA}.[10]

The zeta potential of NAA (ζ_{NAA}) is the potential difference between the bulk ionic electrolyte solution and the shear plane of NAA in that electrolyte (i.e., NAA surface + Helmholtz rigid double layer + Gouy−Chapman double layer).[51] Therefore, this parameter can be considered as a relative indicator of σ_{S-NAA}. Figure 6 (left) depicts the zeta potentials of NAA_{Su}, NAA_{Ox}, and NAA_{Ph} membranes in 0.01 M KCl at pH = 3−10, which are found to decrease linearly with increasing pH. Analysis of these graphs reveals that the IEP_{NAA} of blind-hole NAA membranes produced in sulfuric, oxalic, and phosphoric electrolyte (i.e., pH at which ζ_{NAA} = 0 mV) is 6.0, 5.3, and 4.6, respectively. It has been proposed that NAA membranes feature an asymmetric, hybrid structure consisting of arrays of straight cylindrical nanopores along their thicknesses and much smaller (i.e., 0.0−1.3 nm) ionic nanochannels across their BOLs.[37] The ionic current rectification property seen in blind-hole NAA membranes has been attributed to the gradient in surface charge density and geometric asymmetry between nanopores and ionic nanochannels. However, in such a system ionic current rectification would be expected to be ineffective at the corresponding IEP_{NAA} (i.e., ICR ratio transition from negative to positive at the pH where ζ_{NAA} = 0 mV → σ_{S-NAA} = 0 C·m^{-2}). Analysis of the ICR ratio of NAA_{Su}, NAA_{Ox}, and NAA_{Ph} membranes in 0.1 M KCl at pH = 3−10 shown in Figure 6 (right) reveals a distinct rectification efficiency pattern with pH. Whereas NAA_{Su} and NAA_{Ox} show a Gaussian-like pH dependence of the ICR ratio centered at pH = 6.0, NAA_{Ph} membranes show an exponentially decreasing ICR ratio with a maximum of 37 at pH = 3. These values are close to the estimated values of IEP_{NAA} for each type of blind-hole NAA membrane (i.e., 6.0, 5.3, and 4.6, respectively). However, the ICR ratios of NAA_{Su}, NAA_{Ox}, and NAA_{Ph} membranes in 0.1 M KCl change their rectification directions (i.e., from J_{ON} at V_{app} < 0 V to J_{ON} at V_{app} > 0 V) at pH ∼ 9.5. These observations are in good agreement with those made by Kim and co-workers, who demonstrated that the ICR in NAA_{Ox} membranes is governed by the fixed space charge density gradient ($\nabla\rho_{BOL}$) across the BOL. Therefore, our findings suggest that NAA_{Su}, NAA_{Ox}, and NAA_{Ph} membranes produced under mild anodization conditions at their corresponding self-ordering potentials feature an equivalent $\nabla\rho$ across the volume of their BOL. This result would also indicate that the distribution of fixed negative (O^{2-}) and positive (Al^{3+}) charge vacancies across BOLs of varying thicknesses is determined by the anodization regime and independent of the acid electrolyte. As such, the mechanism by which fixed charge vacancies are generated in the BOL of self-organized NAA membranes would follow an onion-like gradient structure concomitant to that of the incorporation of ionic impurities from the acid electrolyte.[13,52]

3.4. Surface Chemistry Functionalization of Engineered NAA Membranes. Blind-hole NAA membranes produced in oxalic acid electrolyte by the two-step anodization process have been used as iontronic sensing platforms for a variety of analytes.[37−40] To this end, the surface of NAA must be chemically modified with specific functional molecules to attain chemical selectivity toward targeted analytes. For instance, Zhao and co-workers assessed the effect of pH electrolyte on the sensitivity of model NAA_{Ox} membranes to detect thrombin—a blood coagulation serine protease enzyme—through changes in their characteristic ICR signals.[40] Enhancements in sensitivity were attributed to the relative arrangement between the pH of the KCl electrolyte (pH_{KCl}) and the isoelectric point of the analyte molecules immobilized onto the surface of NAA ($IEP_{Analyte}$), using the hybrid nanopore−ionic nanochannel system. The iontronic sensitivity was found to be optimal at pH_{KCl} = 9.0 > $IEP_{Analyte}$ = 7.0−7.4, a configuration under which the flow of cations from the outer to the inner side of the aptamer-functionalized BOL was thought to be enhanced due to increased asymmetry in the surface charge density between nanopores and ionic channels across the BOL. In light of these results, we hypothesize that the sensitivity of this model iontronic system could be maximized by increasing the ICR efficiency of NAA's BOL through structural engineering. To elucidate this question, we decided to use the binding affinity of gold ions (Au^{3+}) in solution with thiol functional groups (-SH) on the surface as a model selective chemical interaction. So, the inner surface of a set of freshly prepared, blind-hole NAA_{Su}, NAA_{Ox}, and NAA_{Ph} membranes (i.e., outer side of BOL) was selectively functionalized with a layer of thiol-containing silane molecules (i.e., MPTMS) (Figure 7a).

In this process, NAA membranes are first hydroxylated to increase the number of available -OH groups on the surface of the anodic oxide. After hydroxylation, a self-assembled monolayer of MPTMS molecules is immobilized onto the inner surface of NAA via wet chemistry. During this step, silane molecules in solution hydrolyze to form silanols, which then readily attach to -OH groups on the surface of the anodic oxide.[53] Upon immobilization, the MPTMS monolayer is subjected to a 1-h-long annealing step at 110 °C to cross-link adjacent silane molecules through an internal polymerization reaction to form Si−O−Si (siloxane) and mechanically consolidate the MPTMS functional layer. Figure 7b shows

https://doi.org/10.1021/acsami.2c02369
ACS Appl. Mater. Interfaces XXXX, XXX, XXX−XXX

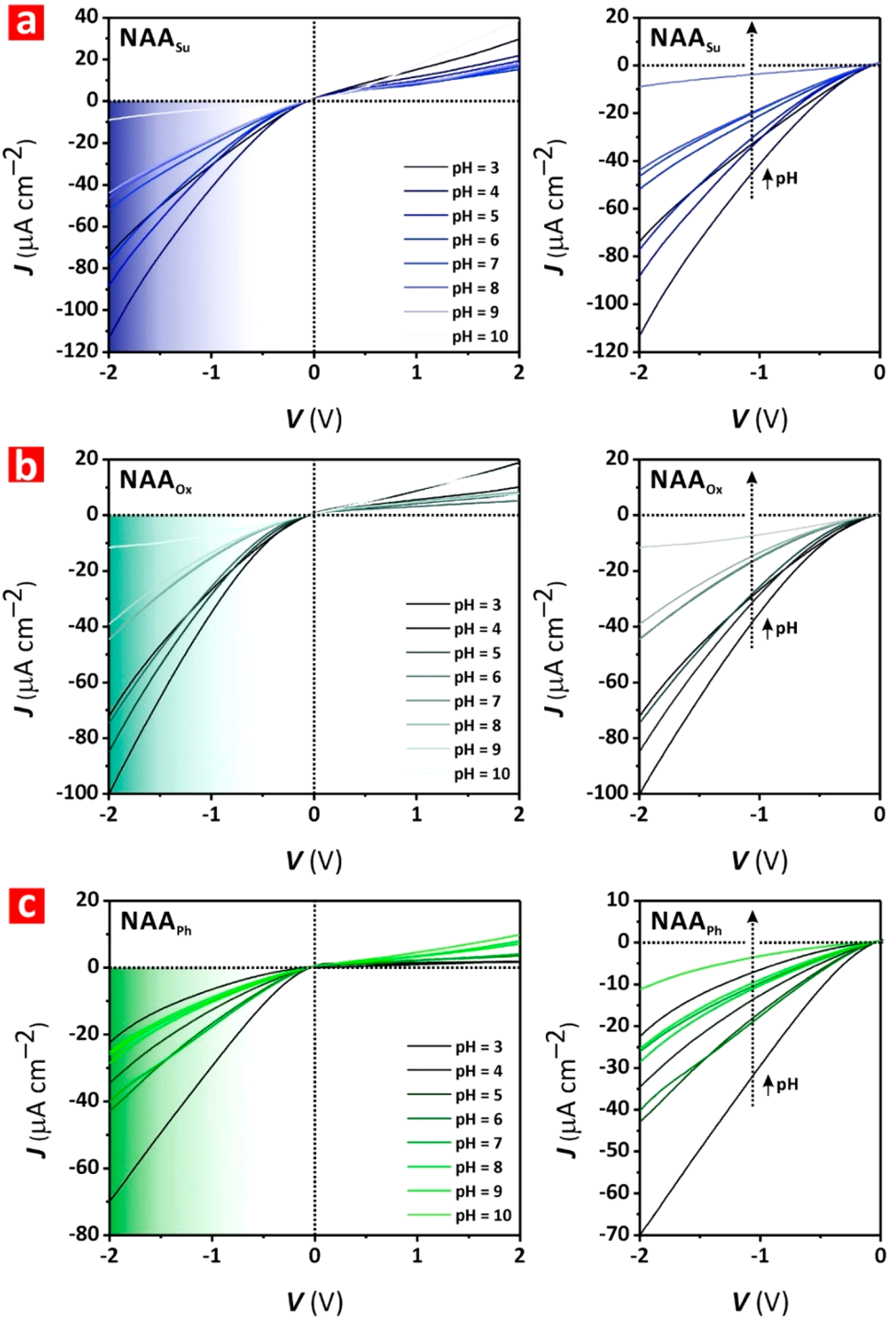

Figure 5. Dependence of ionic current rectification (ICR) on the pH of 0.1 M KCl electrolyte, from 3 to 10, in engineered NAA membranes (NB: all blind-hole NAA membranes were subjected to the reset process prior to $J-V$ characterization). (a) Full (left) and J_{ON} magnified (right) view of the ionic $J-V$ characteristic of a blind-hole NAA_{Su} membrane in 0.1 M KCl at pH = 3−10. (b) Full (left) and J_{ON} magnified (right) view of the ionic $J-V$ characteristic of a blind-hole NAA_{Ox} membrane in 0.1 M KCl at pH = 3−10. (c) Full (left) and J_{ON} magnified (right) view of the ionic $J-V$ characteristic of a blind-hole NAA_{Ph} membrane in 0.1 M KCl at pH = 3−10.

images of the water contact angle measured on the top surface of bare (i) and MPTMS-functionalized (ii) NAA_{Su}, NAA_{Ox}, and NAA_{Ph} membranes. Analysis of the water contact angle indicates that as-produced NAA_{Su}, NAA_{Ox}, and NAA_{Ph} membranes are hydrophilic with a water contact angle that is found to increase with nanopore size (i.e., 17 ± 1, 20 ± 4, and 46 ± 4°, respectively) (Figure 7c).[54,55] The hydrophobic character of these NAA_{Su}, NAA_{Ox}, and NAA_{Ph} membranes increases to 36 ± 2, 50 ± 6, and 66 ± 4°, respectively, after deposition of the functional MPTMS monolayer due to the presence of thiol terminal groups (-SH) on their surfaces. Interestingly, surface chemistry modification also alters the ICR efficiency and polarity of NAA membranes (Figure 7d). For instance, the ICR ratio of as-produced and MPTMS-functionalized, blind-hole NAA membranes in 0.1 M KCl at pH = 6 is measured to be −5 and −2 for NAA_{Su}, −15 and 2 for

https://doi.org/10.1021/acsami.2c02369
ACS Appl. Mater. Interfaces XXXX, XXX, XXX−XXX

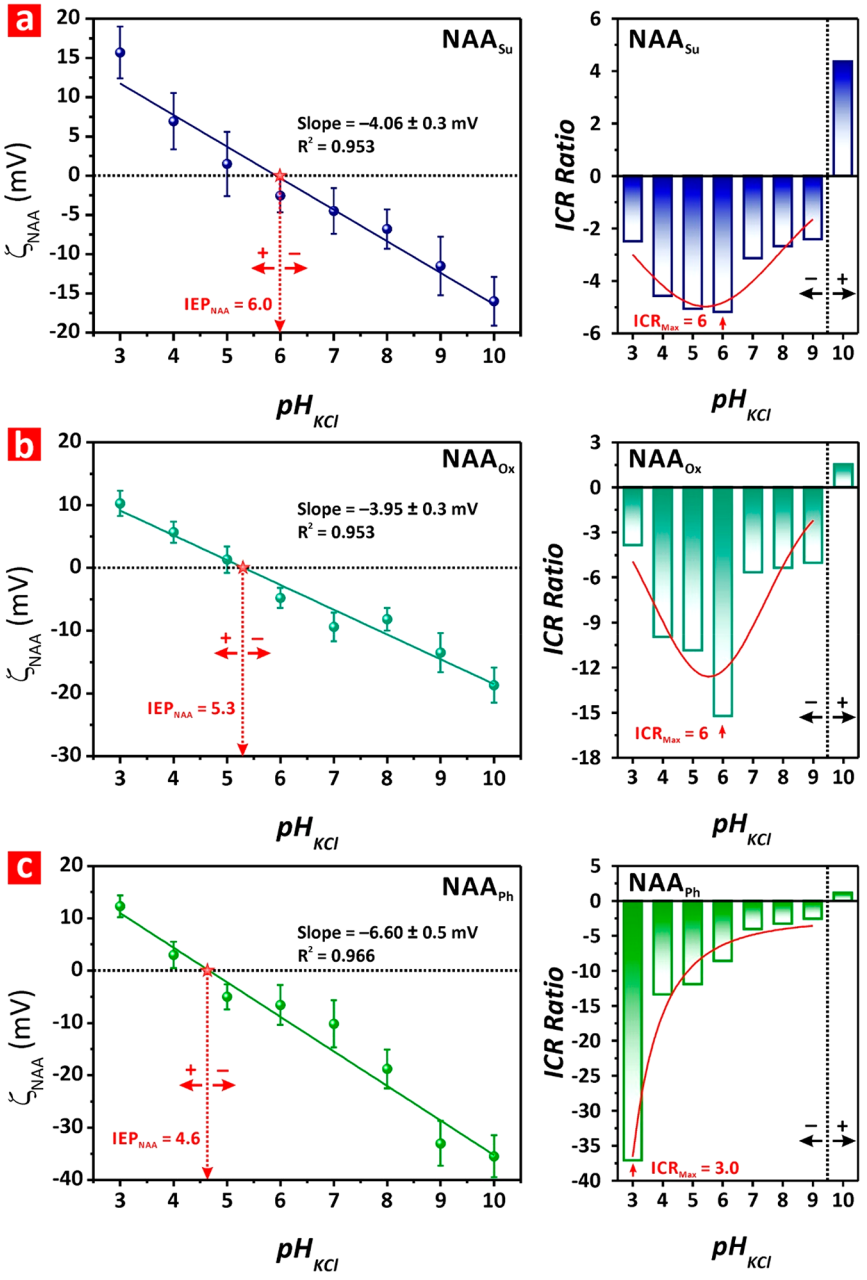

Figure 6. Dependence of the zeta potential (ζ_{NAA}) and ionic current rectification (ICR) ratio in engineered NAA membranes with pH from 3 to 10, in 0.1 M KCl (NB: all blind-hole NAA membranes were subjected to the reset process prior to J–V characterization). (a) ζ_{NAA} (left) and ICR ratio (right) for NAA_{Su} membranes. (b) ζ_{NAA} (left) and ICR ratio (right) for NAA_{Ox} membranes. (c) ζ_{NAA} (left) and ICR ratio (right) for NAA_{Ph} membranes.

NAA_{Ox}, and −11 and 7 for NAA_{Ph}, respectively (Figure S4, Supporting Information). These results indicate that, whereas the polarity of ICR is the same before and after functionalization for NAA_{Su} membranes (i.e., ON state at V_{app} < 0 V), NAA_{Ox} and NAA_{Ph} membranes reverse their rectification direction upon MPTMS modification (i.e., from ON state at V_{app} < 0 V to ON state at V_{app} > 0 V for as-produced and MPTMS-functionalized membranes, respectively). According to the hypothesis proposed by Zhao and co-workers for the detection of thrombin in aptamer-functionalized, blind-hole NAA_{Ox} membranes, the ICR polarity would be determined by the asymmetry in surface charge density (σ_{S-NAA}) between the nanopores and the ionic channels connecting the inner and outer surfaces of the NAA's BOL. Under such a hypothesis, the high ionic conduction state (i.e., J_{ON}) should occur at V_{app} < 0 V when pH_{KCl} < IEP_{NAA} and at V_{app} > 0 V when pH_{KCl} > IEP_{NAA}.[40] It was also postulated that at $pH_{KCl} \approx IEP_{NAA}$ the ICR ratio should be close to 1 and $J_{ON} \approx J_{OFF}$. In principle, this hypothesis would be in good agreement with our estimations of IEP_{NAA} and ICR polarity for MPTMS-functionalized NAA_{Su}, NAA_{Ox}, and NAA_{Ph} membranes at pH 6 (Figure 8).

However, Kim and co-workers recently demonstrated that the gradient of the space charge density across the BOL ($\nabla\rho_{BOL}$) rather than the asymmetry of σ_{S-NAA} between the nanopores and ionic nanochannels crossing the BOL is the governing factor determining the ICR behavior of blind-hole NAA membranes.[13] To gain further insights into this question,

https://doi.org/10.1021/acsami.2c02369
ACS Appl. Mater. Interfaces XXXX, XXX, XXX−XXX

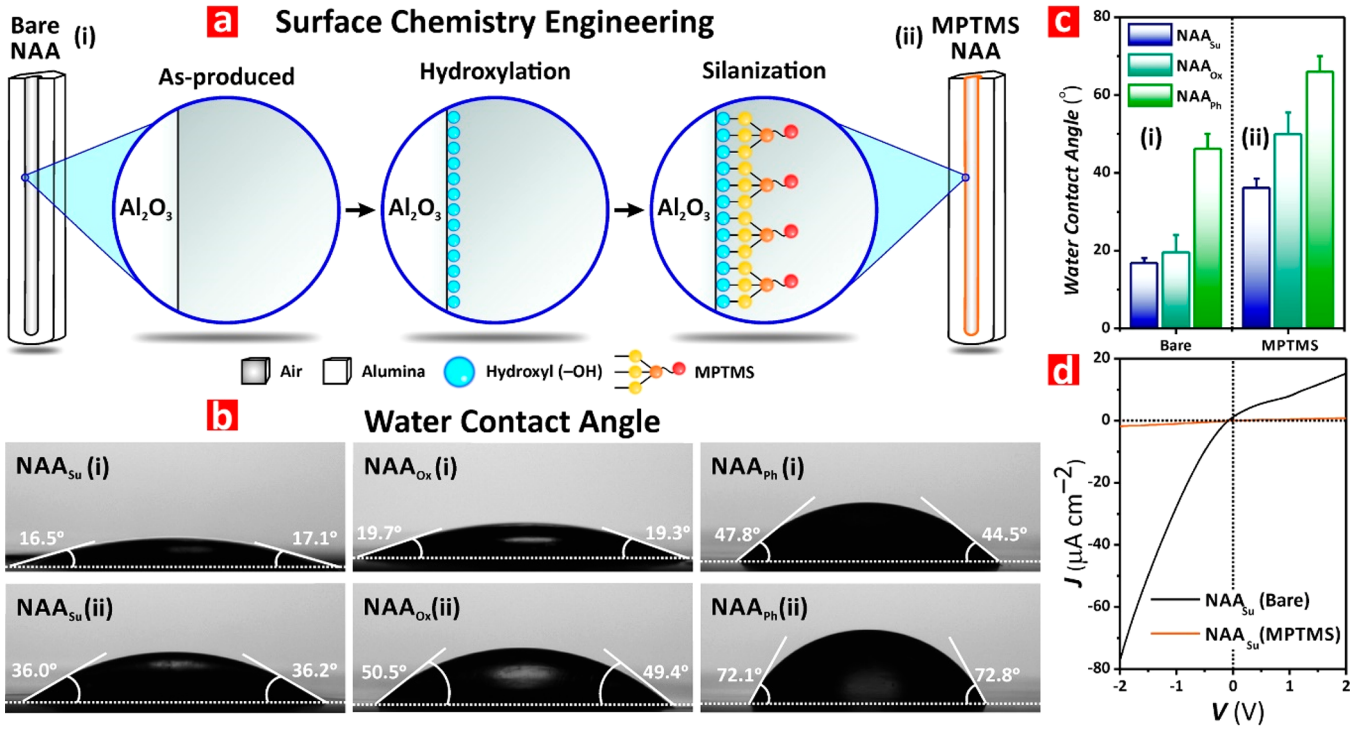

Figure 7. Surface chemistry engineering of NAA membranes produced in sulfuric, oxalic, and phosphoric acid electrolytes (NAA_{Su}, NAA_{Ox}, and NAA_{Ph}) by the two-step anodization process. (a) Schematic describing the wet chemistry process used to selectively immobilize a monolayer of MPTMS on the inner side of blind-hole NAA membranes. (b) Digital images showing representative water contact angle measurements in NAA_{Su}, NAA_{Ox}, and NAA_{Ph} before (i) and after (ii) MPTMS functionalization. (c) Bar chart summarizing the average water contact angle measured in NAA_{Su}, NAA_{Ox}, and NAA_{Ph} before (i) and after (ii) MPTMS functionalization (NB: error bars represent the standard deviation from 10 different measurements). (d) Ionic $J-V$ characteristic of a representative blind-hole NAA_{Su} membrane in 0.1 M KCl at pH = 6 before and after MPTMS functionalization.

we analyzed the dependence of the IEP_{NAA} and $J-V$ characteristic of MPTMS-functionalized, blind-hole NAA_{Su}, NAA_{Ox}, and NAA_{Ph} membranes in a 0.1 M KCl electrolyte at varying pH values, from 3 to 10 (Figure S5, Supporting Information). It is apparent that, in contrast to their as-produced NAA counterparts, the polarity of the ICR ratio for the MPTMS-functionalized systems is reversed at distinct pH (i.e., 8.5, 4.5, and 4.5 for NAA_{Su}, NAA_{Ox}, and NAA_{Ph} membranes, respectively) and it is independent of IEP_{NAA}. The degree of charge of thiol terminal groups (-SH) of MPTMS due to deprotonation is expected to be low at lower pH since -SH is a weak acid that forms a negatively charged conjugate base. The negative potential of NAA membranes at pH 3 is attributed to the preferential adsorption of less hydrolyzable negative ions. The residual hydroxyl groups on NAA that are not bound to MPTMS might be deprotonated in an aqueous solution of KCl at low pH, which might also contribute to the negative zeta potential at pH 3. Although further research will be needed to fully clarify this question, our results would suggest that changes in ICR efficiency and polarity in functionalized NAA membranes could be attributed to a balance between the gradient of σ_{S-NAA} along the nanopores/ionic nanochannels and the space charge density gradient ($\nabla\rho_{BOL}$) across the BOL. For instance, let us assume that the space charge density is uniform at both sides of the BOL; then $\nabla\rho_{BOL}$ can be approximated to the space charge density increment between the inner and outer layers of the BOL (i.e., $\nabla\rho_{BOL} \approx \Delta\rho_{BOL} = \rho_{BOL-inner} - \rho_{BOL-outer}$). If we also consider that the electric field across the BOL ($\nabla\phi_{BOL}$) relies on the space charge density gradient ($\Delta\rho_{BOL}$) and the thickness of the BOL (τ_{BOL}), then we can infer that, for a given potential bias, $\nabla\phi_{BOL}$ will decrease following the order NAA_{Su} > NAA_{Ox} > NAA_{Ph}. Under such conditions, the ICR polarity should be determined by the BOL when the influence of $\nabla\phi_{BOL}$ is stronger than that of σ_{S-NAA} along the nanopore/ionic nanochannels. On the other hand, if the influence of σ_{S-NAA} is stronger than that of $\nabla\phi_{BOL}$, the ICR behavior should be governed by the surface charge density along the nanopore/ionic nanochannels. This hypothesis would in principle explain our observations on the transport of K^+ and Cl^- ions across MPTMS-functionalized, blind-hole NAA membranes with varying BOL thicknesses and the associated and high ionic conduction states, where the transduction mechanism is determined by the space charge density in the NAA_{Su} membrane (i.e., thinner BOL) and by the surface charge density gradient between nanopores and ionic channels in NAA_{Ox} and NAA_{Ph} membranes (i.e., thicker BOL), respectively (Figure 8).

3.5. Iontronic Sensing of Gold(III) Ions in Engineered NAA Membranes. To elucidate the effect of NAA's BOL on the sensing performance of this model iontronic platform, MPTMS-functionalized NAA membranes produced in sulfuric, oxalic, and phosphoric acid electrolyte were exposed to analytical solutions of gold(III) ions (Au^{3+}) of varying concentrations, from 0 to 300 μM. Figure 9 shows how the $J-V$ characteristic of blind-hole NAA_{Su}, NAA_{Ox}, and NAA_{Ph} membranes changes dynamically upon exposure to Au^{3+} solutions of increasing concentrations. It is apparent that binding of Au^{3+} ions to the functional MPTMS layer on the inner surface of NAA membranes decreases ionic transport

https://doi.org/10.1021/acsami.2c02369
ACS Appl. Mater. Interfaces XXXX, XXX, XXX−XXX

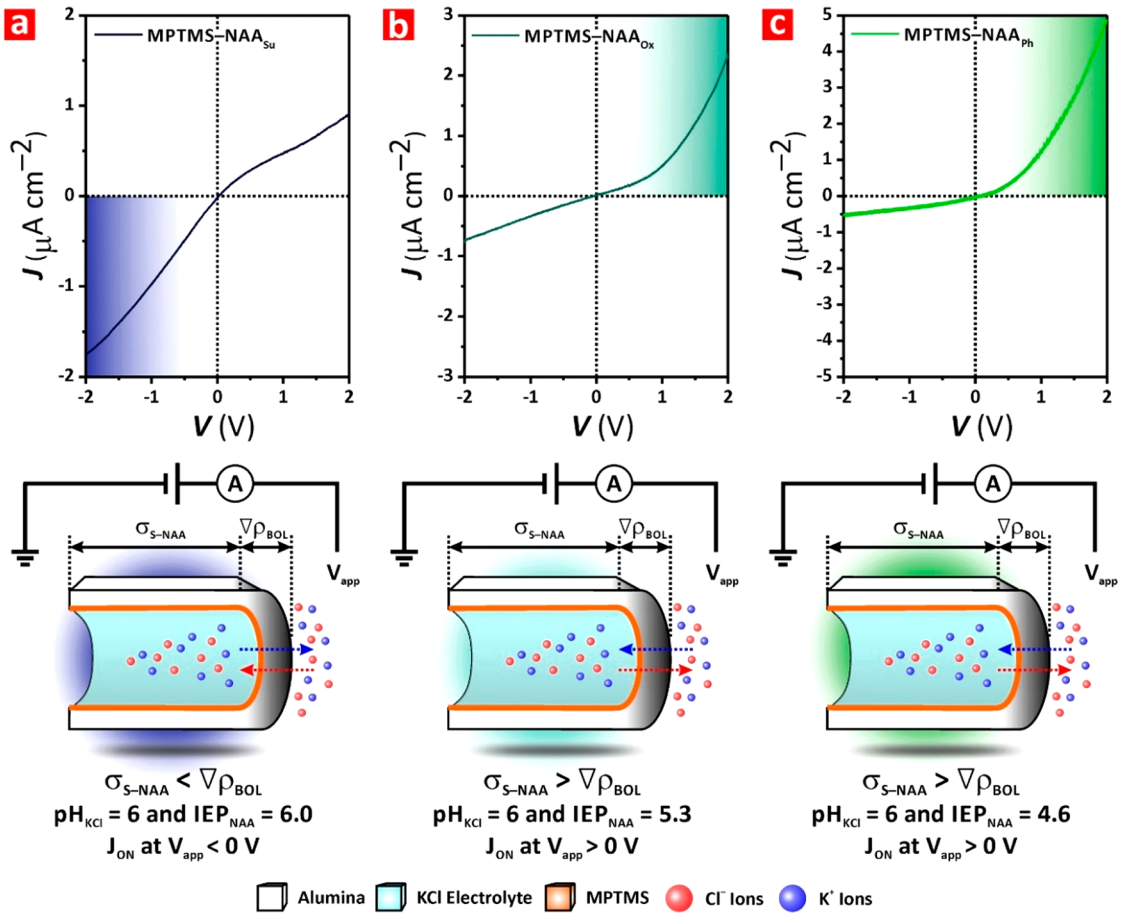

Figure 8. Understanding ionic flow transport across MPTMS-functionalized NAA membranes produced in sulfuric, oxalic, and phosphoric acid electrolytes (NAA_{Su}, NAA_{Ox}, and NAA_{Ph}) by the two-step anodization process. (a) Ionic $J-V$ characteristic of a MPTMS-functionalized, blind-hole NAA_{Su} membrane in 0.1 M KCl at pH = 6 (top) and schematic describing the ionic flow mechanism across the BOL (bottom). (b) Ionic $J-V$ characteristic of a MPTMS-functionalized, blind-hole NAA_{Ox} membrane in 0.1 M KCl at pH = 6 (top) and schematic describing the ionic flow mechanism across the BOL (bottom). (c) Ionic $J-V$ characteristic of a MPTMS-functionalized, blind-hole NAA_{Ph} membrane in 0.1 M KCl at pH = 6 (top) and schematic describing the ionic flow mechanism across the BOL (bottom).

across the BOL with increasing [Au^{3+}]. After MPTMS functionalization, the functional layer of MPTMS molecules on the inner surface of NAA's nanopores acts as an additional hindrance for ion transport across the BOL. In the case of KCl electrolyte, this functional layer increases the overall resistance of the system (i.e., reduction of J_{ON} and J_{OFF} values) by reducing the flow of K^+ and Cl^- ions through the BOL due to surface charge modification and reduction of ionic channel size. When Au^{3+} ions are added into one of the electrolytes of the H-cell, these are immobilized by the thiol terminals of MPTMS functional molecules. This interaction further increases the steric hindrance effect and limits transport of K^+ and Cl^- ions across the BOL (i.e., indicated by a reduction of J_{ON}). As such, the overall resistance for ionic transport across the BOL increases and the ionic transport across the BOL decreases. Hence, there is a decreased ionic current rectification as [Au^{3+}] increases.[54] These results are in good agreement with those reported by Zhao and co-workers for the detection of Cu^{2+} ions in PGA-modified, blind-hole NAA_{Ox} membranes.[38] However, analysis of the $J-V$ characteristic reveals apparent differences between NAA membranes with distinct BOLs.

Figure 9a shows that both J_{ON} and J_{OFF} decrease in absolute value with increasing [Au^{3+}] in NAA_{Su} membranes, where J_{ON} = −1.8 and −1.2 μA cm^{-2} and J_{OFF} = 0.9 and 0.8 μA cm^{-2} at [Au^{3+}] = 0 and 300 μM, respectively. NAA_{Ox} membranes also show a similar trend to that of NAA_{Su} membranes but of opposite polarity, where J_{ON} = 2.3 and 0.9 μA cm^{-2} and J_{OFF} = −0.8 and −0.7 μA cm^{-2} at [Au^{3+}] = 0 and 300 μM, respectively (Figure 9b). NAA_{Ph} membranes also show decreasing ionic conduction with increasing analyte concentration, with J_{ON} = 4.9 and 2.4 μA cm^{-2} and J_{OFF} = −0.6 and −0.4 μA cm^{-2} at [Au^{3+}] = 0 and 300 μM, respectively (Figure 9c). These results indicate that, for a specific binding reaction, an increment in ionic rectification associated with increasing BOL thickness is translated into an enhancement of sensitivity when Au^{3+} ions are immobilized onto the functional layer due to additional ionic resistance. To gain further insights into this question, we determined the sensing performance for this model binding reaction in MPTMS-functionalized, blind-hole NAA membranes. Figure 10 depicts the dependence of J_{ON} with [Au^{3+}] for NAA_{Su}, NAA_{Ox}, and NAA_{Ph} membranes, including linear fittings used to determine key sensing parameters such as sensitivity (S), linearity (R^2), and low limit of detection (LoD). These chemically selective iontronic platforms show two sensing regimes: one at low concentration (LC), from 0 to 3 × 10^{-6} μM, and another one at high concentration (HC), from 75 to 300 μM. Analysis of these sensing parameters summarized in Table 4 reveals that the sensitivity of the system increases with increasing BOL

https://doi.org/10.1021/acsami.2c02369
ACS Appl. Mater. Interfaces XXXX, XXX, XXX−XXX

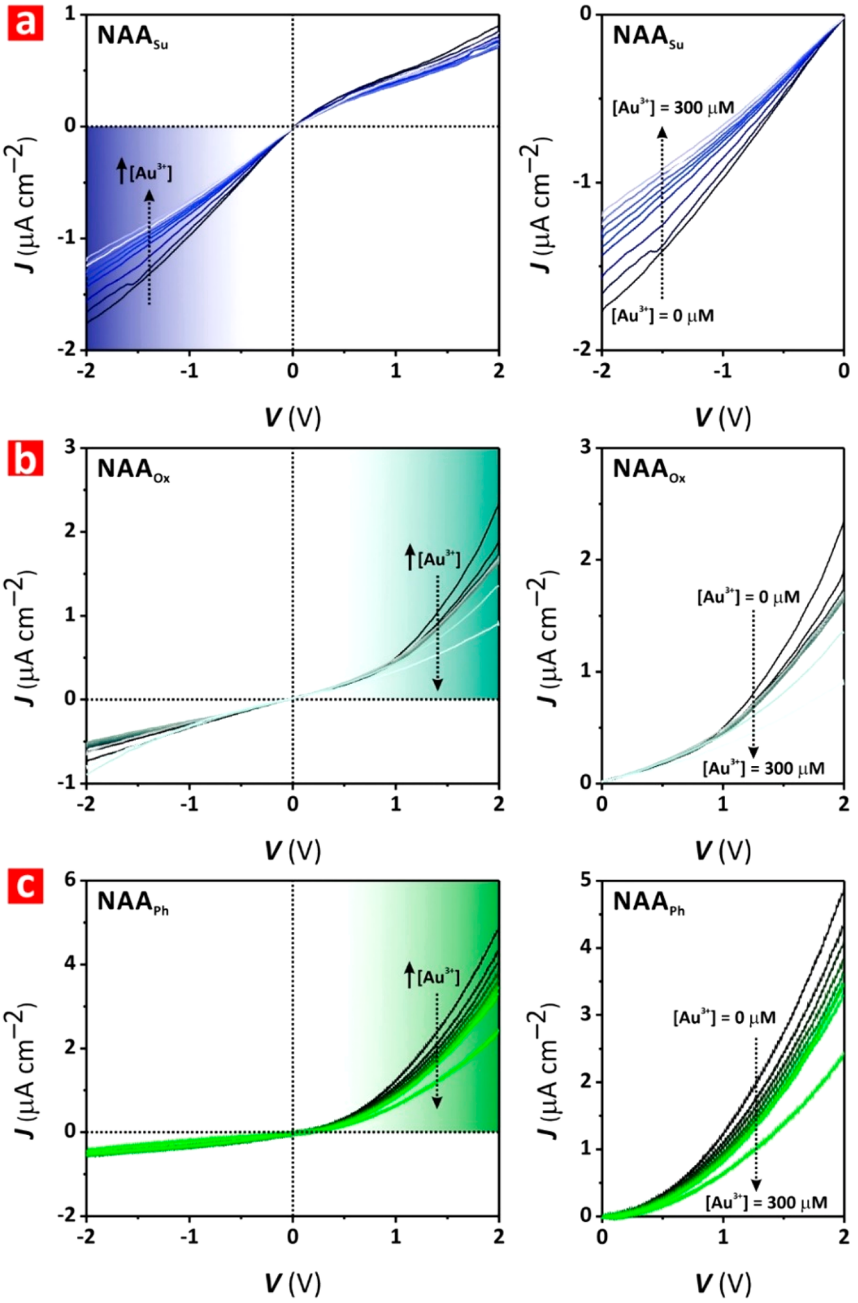

Figure 9. Dynamic changes in the ionic $J-V$ characteristic of MPTMS-functionalized, blind-hole NAA_{Su}, NAA_{Ox}, and NAA_{Ph} membranes upon exposure to analytical solutions of gold ions (Au^{3+}) with varying concentrations, from 0 to 300 μM. (a) Full (left) and J_{ON} magnified (right) view of the $J-V$ characteristic of MPTMS-functionalized NAA_{Su} membranes with varying [Au^{3+}]. (b) Full (left) and J_{ON} magnified (right) view of the $J-V$ characteristic of MPTMS-functionalized NAA_{Ox} membranes with varying [Au^{3+}]. (c) Full (left) and J_{ON} magnified (right) view of the $J-V$ characteristic of MPTMS-functionalized NAA_{Ph} membranes with varying [Au^{3+}].

thickness for both concentration ranges. However, it is apparent that the system is much more sensitive at the low compared to the high concentration regime. The absolute value of S in the LC range is measured to be 0.13 ± 0.02, 0.19 ± 0.04, and 0.44 ± 0.04 (μA cm^{-2}) pM^{-1} for NAA_{Su}, NAA_{Ox}, and NAA_{Ph} membranes, respectively. Although the system shows the same trend with increasing BOL thickness in the HC range, the absolute value of S is several orders of magnitude lower than that estimated for the LC range (i.e., $(2.8 \pm 2.0) \times 10^{-4}$, $(3.4 \pm 0.8) \times 10^{-3}$, and $(4.4 \pm 0.2) \times 10^{-3}$ (μA cm^{-2}) μM^{-1} for NAA_{Su}, NAA_{Ox}, and NAA_{Ph} membranes, respectively).

At low [Au^{3+}] range, the number of Au^{3+} ions in solution allows an effective interaction with thiol groups in MPTMS molecules immobilized onto the inner side of NAA nanopores. Under such conditions, Au^{3+} ions are free to interact and bind with thiol functional groups. However, excess Au^{3+} ions in solution within the HC range hinder this binding interaction due to competing binding between Au^{3+} ions, which in turn reduces the overall sensitivity of the system. It is also important to note that lower sensitivity is expected in the proximity of the saturation range (i.e., range of concentration in which the binding interaction is saturated and thus independent of the concentration of analyte). Indeed, analysis of the LoD also

https://doi.org/10.1021/acsami.2c02369
ACS Appl. Mater. Interfaces XXXX, XXX, XXX−XXX

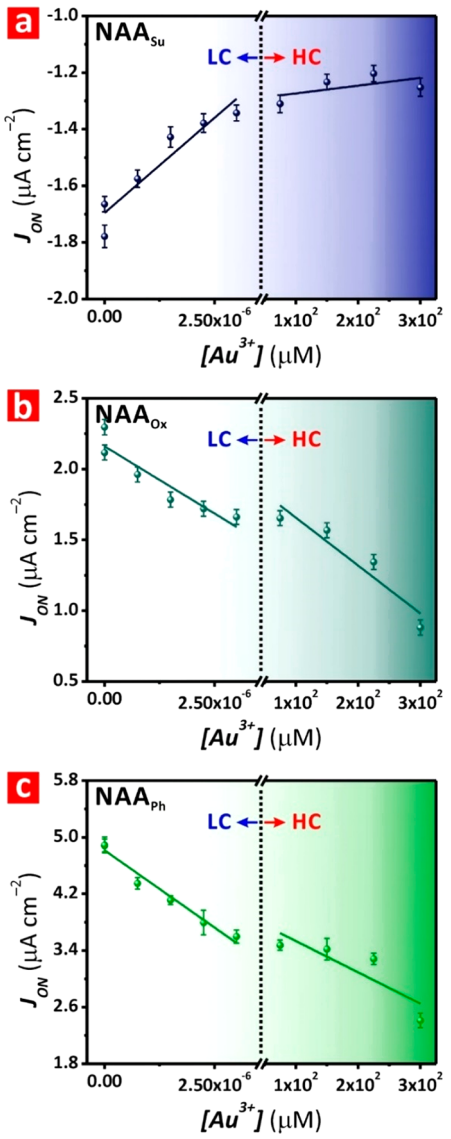

Figure 10. Summary of the chemical sensitivity of MPTMS-functionalized, blind-hole NAA_{Su}, NAA_{Ox}, and NAA_{Ph} membranes for the detection of gold ions (Au^{3+}) with varying concentrations, from 0 to 300 μM (NB: LC = low concentration and HC = high concentration). (a) Dependence of J_{ON} with [Au^{3+}] for MPTMS-functionalized NAA_{Su} membranes. (b) Dependence of J_{ON} with [Au^{3+}] for MPTMS-functionalized NAA_{Ox} membranes. (c) Dependence of J_{ON} with [Au^{3+}] for MPTMS-functionalized NAA_{Ph} membranes.

indicates that this iontronic system performs much better at low concentrations, achieving remarkably low limits of detection within the sub-picomolar range (i.e., 0.8, 0.9, and 0.4 pM for NAA_{Su}, NAA_{Ox}, and NAA_{Ph} membranes, respectively). It is also found that the correlation of J_{ON} with the concentration of analyte is much stronger for the LC regime than that of the HC range, with average linearity values of 0.896 and 0.709, respectively. These results demonstrate that engineering the characteristics of the BOL in NAA membranes is a critical aspect to consider in the design of iontronic sensing systems based on these nanoporous platforms. The sensitivity of this system is found to increase with increasing BOL thickness (i.e., 0.0015 (μA cm^{-2}) pM^{-1} per nm of BOL for the LC range) and ICR rectification efficiency. This finding provides new opportunities to develop ultrasensitive, label-free sensing platforms with broad applicability across nanofluidic and iontronic applications.

4. CONCLUSIONS

We have investigated the ionic current rectification characteristics across three types of NAA membranes fabricated by the two-step anodization process in sulfuric, oxalic, and phosphoric acid electrolytes at their corresponding self-organization potentials. All these model blind-hole NAA membranes showed a characteristic ICR behavior, which was found to rely on the geometric properties of the BOL at their nanopore bottom tips. Interestingly, all NAA membranes showed inversion of ICR polarity at pH = 9.5, conditions under which the high ionic conduction state changed from negative to positive polarity. In all cases, the maximum of rectification efficiency or ICR ratio was found to be below that pH at which the ICR polarity changes. This result would suggest that NAA membranes produced under self-organization conditions feature the same distribution of positive and negative fixed charge vacancies across the thicknesses of their BOLs. As such, we hypothesized that it is possible to maximize the sensitivity of this iontronic system by engineering the characteristics of the BOL. To elucidate this question, we used the chemical affinity of gold ions to thiol functional groups as a model reaction. MPTMS-functionalized NAA membranes with varying BOLs were exposed to analytical solutions of gold ions. The ICR characteristic of these blind-hole membranes underwent dynamic changes upon exposure to increasing concentrations of gold ions. Analysis of sensing performance using changes in the current density at the high ionic conduction state as the core sensing principle revealed two working ranges, at low and high analyte concentration. The low limit of detection of the system at these regimes is at the pico- and micromolar levels, respectively. It was also found that the sensitivity of this system increases linearly with the BOL

Table 4. Summary of Sensing Parameters of MPTMS-Functionalized NAA Membranes Produced in Sulfuric, Oxalic, and Phosphoric Acid Electrolytes (NAA_{Su}, NAA_{Ox}, and NAA_{Ph}) for the Detection of Gold Ions (Au^{3+}) within Low and High Concentration Ranges[a]

	LC			HC		
NAA	S[c] ((μA cm^{-2}) pM^{-1})	R^2	LoD[b] (pM)	S[c] ((μA cm^{-2}) μM^{-1})	R^2	LoD[b] (μM)
NAA_{Su}	0.13 ± 0.02	0.873	0.8	(2.8 ± 2.0)×10^{-4}	0.656	75
NAA_{Ox}	−0.19 ± 0.04	0.850	0.9	−(3.4 ± 0.8)×10^{-3}	0.850	75
NAA_{Ph}	−0.44 ± 0.04	0.964	0.4	−(4.4 ± 0.2)×10^{-3}	0.621	75

[a] $[Au^{3+}]_{LC}$ = 0−3 × 10^{-6} μM and $[Au^{3+}]_{HC}$ = 75−300 μM. [b] Estimated as $3\sigma = (3 \cdot STD_{Intercept})/S$. [c] Negative value of S indicates that J_{ON} occurs at V_{app} > 0 V and *vice versa* for positive values of S.

https://doi.org/10.1021/acsami.2c02369
ACS Appl. Mater. Interfaces XXXX, XXX, XXX−XXX

thickness at a rate of 0.0015 (μA cm^{-2}) pM^{-1} per nm of BOL for the low concentration range. As such, the thicker the BOL, the more sensitive the iontronic NAA membrane is. Our findings provide new avenues for developing cutting-edge iontronic technologies based on NAA structures, which could find broad applicability across multiple disciplines such as energy conversion, sensing, nanofluidics, and biomimicking information transduction.

■ ASSOCIATED CONTENT

Supporting Information

The Supporting Information is available free of charge at https://pubs.acs.org/doi/10.1021/acsami.2c02369.

Additional experimental details and characterizations of the iontronic system setup, images of epoxy coated NAA membranes and area determination of the unmasked region of NAA membranes, the reset process, Nyquist impedance spectroscopy spectra for as-produced blind-hole NAA membranes, and ionic current rectification characteristic for these membranes before and after MPTMS functionalizationpap (PDF)

■ AUTHOR INFORMATION

Corresponding Authors

Cheryl Suwen Law − *School of Chemical Engineering and Advanced Materials, The University of Adelaide, South Australia 5005 Adelaide, Australia; Institute for Photonics and Advanced Sensing, The University of Adelaide, South Australia 5005 Adelaide, Australia; Monash Institute of Pharmaceutics Science, Monash University, Victoria 3052 Melbourne, Australia*; Email: suwen.law@adelaide.edu.au

Andrew D. Abell − *Institute for Photonics and Advanced Sensing and Department of Chemistry, The University of Adelaide, South Australia 5005 Adelaide, Australia*; orcid.org/0000-0002-0604-2629; Email: andrew.abell@adelaide.edu.au

Abel Santos − *School of Chemical Engineering and Advanced Materials, The University of Adelaide, South Australia 5005 Adelaide, Australia; Institute for Photonics and Advanced Sensing, The University of Adelaide, South Australia 5005 Adelaide, Australia*; orcid.org/0000-0002-5081-5684; Email: abel.santos@adelaide.edu.au

Authors

Juan Wang − *School of Chemical Engineering and Advanced Materials, The University of Adelaide, South Australia 5005 Adelaide, Australia; Institute for Photonics and Advanced Sensing, The University of Adelaide, South Australia 5005 Adelaide, Australia*

Satyathiran Gunenthiran − *School of Chemical Engineering and Advanced Materials, The University of Adelaide, South Australia 5005 Adelaide, Australia; Institute for Photonics and Advanced Sensing, The University of Adelaide, South Australia 5005 Adelaide, Australia*

Huong Nguyen Que Tran − *School of Chemical Engineering and Advanced Materials, The University of Adelaide, South Australia 5005 Adelaide, Australia; Institute for Photonics and Advanced Sensing, The University of Adelaide, South Australia 5005 Adelaide, Australia*; orcid.org/0000-0002-8309-262X

Khoa Nhu Tran − *School of Chemical Engineering and Advanced Materials, The University of Adelaide, South Australia 5005 Adelaide, Australia; Institute for Photonics and Advanced Sensing, The University of Adelaide, South Australia 5005 Adelaide, Australia*; orcid.org/0000-0001-5812-2463

Siew Yee Lim − *School of Chemical Engineering and Advanced Materials, The University of Adelaide, South Australia 5005 Adelaide, Australia; Institute for Photonics and Advanced Sensing, The University of Adelaide, South Australia 5005 Adelaide, Australia*

Complete contact information is available at: https://pubs.acs.org/10.1021/acsami.2c02369

Notes

The authors declare no competing financial interest.

■ ACKNOWLEDGMENTS

The authors would like to acknowledge and pay their respects to the Kaurna−Adelaide people, the Traditional Custodians of the land on which the work was performed. The authors acknowledge the support provided by the Australian Research Council through the grants DP200102614 and DP220102857, the School of Chemical Engineering and Advanced Materials, The University of Adelaide, the Institute for Photonics and Advanced Sensing (IPAS), and the ARC Centre of Excellence for Nanoscale BioPhotonics (CNBP).

■ REFERENCES

(1) Lee, W.; Park, S. J. Porous Anodic Aluminum Oxide: Anodization and Templated Synthesis of Functional Nanostructures. *Chem. Rev.* **2014**, *114*, 7487−7556.

(2) Sulka, G. D. Highly Ordered Anodic Porous Alumina Formation by Self-Organized Anodizing. In *Nanostructured Materials in Electrochemistry*; Eftekhari, A., Ed.; Wiley-VCH Verlag Gmbh&Co. KGaA: Weinheim, 2008; Vol. *1*, Chapter 1, p 1.

(3) Losic, D., Santos, A., Eds. *Nanoporous Alumina: Fabrication, Structure, Properties and Applications*; Springer International Publishing: Switzerland, 2015.

(4) Keller, F.; Hunter, M. S.; Robinson, D. L. Structural Features of Oxide Coatings on Aluminum. *J. Electrochem. Soc.* **1953**, *100*, 411−419.

(5) Shimizu, K.; Kobayashi, K.; Thompson, G. E.; Wood, G. C. Development of Porous Anodic Films on Aluminium. *Philos. Mag. A* **1992**, *66*, 643−652.

(6) Thompson, G. E. Porous Anodic Alumina: Fabrication, Characterization and Applications. *Thin Solid Films* **1997**, *297*, 192−201.

(7) Van Overmeere, Q.; Blaffart, F.; Proost, J. What Controls The Pore Spacing in Porous Anodic Oxides? *Electrochem. Commun.* **2010**, *12*, 1174−1176.

(8) Thompson, G. E.; Wood, G. C. Porous anodic film formation on aluminium. *Nature* **1981**, *290*, 230−232.

(9) Vrublevsky, I.; Parkoun, V.; Schreckenbach, J.; Goedel, W. A. Dissolution Behaviour of the Barrier Layer of Porous Oxide Films on Aluminum Formed in Phosphoric Acid Studied by a Re-Anodizing Technique. *Appl. Surf. Sci.* **2006**, *252*, 5100−5108.

(10) Benfedda, B.; Hamadou, L.; Benbrahim, N.; Kadri, A.; Chainet, E.; Charlot, F. Electrochemical Impedance Investigation of Anodic Alumina Barrier Layer. *J. Electrochem. Soc.* **2012**, *159*, C372−C381.

(11) Lou, H.-R.; Tsai, D.-S.; Chou, C.-C. Correlation between Defect Density and Corrosion Parameter of Electrochemically Oxidized Aluminum. *Coatings* **2020**, *10* (1), 20.

(12) Han, H.; Park, S.-J.; Jang, J. S.; Ryu, H.; Kim, K. J.; Baik, S.; Lee, W. In Situ Determination of the Pore Opening Point during Wet-Chemical Etching of the Barrier Layer of Porous Anodic Aluminum Oxide: Nonuniform Impurity Distribution in Anodic Oxide. *ACS Appl. Mater. Interfaces* **2013**, *5*, 3441−3448.

(13) Kim, Y. D.; Choi, S.; Kim, A.; Lee, W. Ionic Current Rectification of Porous Anodic Aluminum Oxide (AAO) with a Barrier Oxide Layer. *ACS Nano* **2020**, *14*, 13727−13738.
(14) González-Castaño, M.; Döbeli, M.; Araullo-Peters, V.; Jeurgens, L. P. H.; Schmutz, P.; Cancellieri, C. Substrate Purity Effect on the Defect Formation and Properties of Amorphous Anodic Barrier Al_2O_3. *J. Electrochem. Soc.* **2018**, *165*, C422−C431.
(15) Shi, W.; Shen, Y.; Ge, D.; Xue, M.; Cao, H.; Huang, S.; Wang, J.; Zhang, G.; Zhang, F. Functionalized Anodic Aluminum Oxide (AAO) Membranes for Affinity Protein Separation. *J. Membr. Sci.* **2008**, *325*, 801−808.
(16) Wu, S.; Wildhaber, F.; Vazquez-Mena, O.; Bertsch, A.; Brugger, J.; Renaud, P. Facile Fabrication of Nanofluidic Diode Membranes using Anodic Aluminium Oxide. *Nanoscale* **2012**, *4*, 5718−5723.
(17) Sui, X.; Zhang, Z.; Zhang, Z.; Wang, Z.; Li, C.; Yuan, H.; Gao, L.; Wen, L.; Fan, X.; Yang, L.; Zhang, X.; Jiang, L. Biomimetic Nanofluidic Diode Composed of Dual Amphoteric Channels Maintains Rectification Direction over a Wide pH Range. *Angew. Chem., Int. Ed.* **2016**, *55*, 13056−13060.
(18) Li, C.-Y.; Ma, F.-X.; Wu, Z.-Q.; Gao, H.-L.; Shao, W.-T.; Wang, K.; Xia, X.-H. Solution-pH-Modulated Rectification of Ionic Current in Highly Ordered Nanochannels Arrays Patterned with Chemical Functional Groups at Designed Positions. *Adv. Funct. Mater.* **2013**, *23*, 3836−3844.
(19) Zhang, Q.; Liu, Z.; Wang, K.; Zhai, J. Organic/Inorganic Hybrid Nanochannels Based on Polypyrrole-Embedded Alumina Nanopore Arrays: pH- and Light-Modulated Ion Transport. *Adv. Funct. Mater.* **2015**, *25*, 2091−2098.
(20) Kong, Y.; Fan, X.; Zhang, M.-H.; Hou, X.; Liu, Z.-Y.; Zhai, J.; Jiang, L. Nanofluidic Dioded Based on Branched Alumina Nanochannels with Tunable Ionic Rectification. *ACS Appl. Mater. Interfaces* **2013**, *5*, 7931−7936.
(21) Zhang, M.; Hou, X.; Wang, J.; Tian, Y.; Fan, X.; Zhai, J.; Jiang, L. Light and pH Cooperative Nanofluidic Diode Using a Spiropyran-Functionalized Single Nanochannel. *Adv. Mater.* **2012**, *24*, 2424−2428.
(22) Chun, H.; Chung, T. D. Iontronics. *Annu. Rev. Anal. Chem.* **2015**, *8*, 441−462.
(23) Tardella, A.; Chazalviel, J.-N. Highly Accumulated Electron Layer at a Semiconductor/Electrolyte Interface. *Phys. Rev. B* **1985**, *32*, 2439−2448.
(24) Lovreček, B.; Despic, A.; Bockris, J. O. M. Electrolytic Junctions with Rectifying Properties. *J. Phys. Chem.* **1959**, *63*, 750−751.
(25) Kou, S.; Lee, H. N.; van Noort, D.; Swamy, K. M. K.; Kim, S. H.; Soh, J. H.; Lee, K.-M.; Nam, S.-W.; Yoon, J.; Park, S. Fluorescent Molecular Logic Gates Using Microfluidic Devices. *Angew. Chem., Int. Ed.* **2008**, *47*, 872−876.
(26) Zhan, W.; Crooks, R. M. Microelectrochemical Logic Circuits. *J. Am. Chem. Soc.* **2003**, *125*, 9934−9935.
(27) Genot, A. J.; Bath, J.; Turberfield, A. J. Reversible Logic Circuits Made of DNA. *J. Am. Chem. Soc.* **2011**, *133*, 20080−20083.
(28) Zhang, H.; Hou, X.; Zeng, L.; Yang, F.; Li, L.; Yan, D.; Tian, Y.; Jiang, L. Bioinspired Artificial Single Ion Pump. *J. Am. Chem. Soc.* **2013**, *135*, 16102−16110.
(29) van der Heyden, F. H. J.; Bonthuis, D. J.; Stein, D.; Meyer, C.; Dekker, C. Power Generation by Pressure-Driven Transport of Ions in Nanofluidic Channels. *Nano Lett.* **2007**, *7*, 1022−1025.
(30) Liu, N.; Jiang, Y.; Zhou, Y.; Xia, F.; Guo, W.; Jiang, L. Two-Way Nanopore Sensing of Sequence-Specific Oligonucleotides and Small-Molecule Targets in Complex Matrices Using Integrated DNA Supersandwich Structures. *Angew. Chem. Int. Ed* **2013**, *52*, 2007−2011.
(31) Siwy, Z.; Heins, E.; Harrell, C. C.; Kohli, P.; Martin, C. R. Conical-Nanotube Ion-Current Rectifiers: The Role of Surface Charge. *J. Am. Chem. Soc.* **2004**, *126*, 10850−10851.
(32) Harrell, C. C.; Kohli, P.; Siwy, Z.; Martin, C. R. DNA-Nanotube Artificial Ion Channels. *J. Am. Chem. Soc.* **2004**, *126*, 15646−15647.
(33) Ali, M.; Ramirez, P.; Nguyen, H. Q.; Nasir, S.; Cervera, J.; Mafe, S.; Ensinger, W. Single Cigar-Shaped Nanopores Functionalized with Amphoteric Amino Acid Chaing: Experimental and Theoretical Characterization. *ACS Nano* **2012**, *6*, 3631−3640.
(34) Cheng, L.-J.; Guo, L. J. Ionic Current Rectification, Breakdown, and Switching in Heterogeneous Oxide Nanofluidic Devices. *ACS Nano* **2009**, *3*, 575−584.
(35) Yameen, B.; Ali, M.; Neumann, R.; Ensinger, W.; Knoll, W.; Azzaroni, O. Ionic Transport through Single Solid-State Nanopores Controlled with Thermally Nanoactuated Macromolecular Gates. *Small* **2009**, *5*, 1287−1291.
(36) Lan, W.-J.; Holden, D. A.; White, H. S. Pressure-Dependent Ion Current Rectification in Conical-Shaped Glass Nanopores. *J. Am. Chem. Soc.* **2011**, *133*, 13300−13303.
(37) Cao, J.; Zhao, X.-P.; Younis, M. R.; Li, Z.-Q.; Xia, X.-H.; Wang, C. Ultrasensitive Capture, Detection, and Release of Circulating Tumor Cells Using a Nanochannel-Ion Channel Hybrid Coupled with Electrochemical Detection Technique. *Anal. Chem.* **2017**, *89*, 10957−10964.
(38) Zhao, X.-P.; Wang, S.-S.; Younis, M. R.; Xia, X.-H.; Wang, C. Asymmetric Nanochannel-Ionchannel Hybrid for Ultrasensitive and Label-Free Detection of Copper Ions in Blood. *Anal. Chem.* **2018**, *90*, 896−902.
(39) Zhao, X.-P.; Liu, F.-F.; Hu, W.-C.; Younis, M. R.; Wang, C.; Xia, X.-H. Biomimetic Nanochannel-Ionchannel Hybrid for Ultrasensitive and Label-Free Detection of MicroRNA in Cells. *Anal. Chem.* **2019**, *91*, 3582−3589.
(40) Zhao, X.-P.; Zhou, Y.; Zhang, Q.-W.; Yang, D.-R.; Wang, C.; Xia, X.-H. Nanochannel-Ion Channel Hybrid Device for Ultrasensitive Monitoring of Biomolecular Recognition Events. *Anal. Chem.* **2019**, *91*, 1185−1193.
(41) Masuda, H.; Fukuda, K. Ordered Metal Nanohole Arrays Made by a Two-Step Replication of Honeycomb Structures of Anodic Alumina. *Science* **1995**, *268*, 1466−1468.
(42) Masuda, H.; Hasegwa, F.; Ono, S. Self-Ordering of Cell Arrangement of Anodic Porous Alumina Formed in Sulfuric Acid Solution. *J. Electrochem. Soc.* **1997**, *144*, L127−L130.
(43) Masuda, H.; Yada, K.; Osaka, A. Self-Ordering of Cell Configuration of Anodic Porous Alumina with Large-Size Pores in Phosphoric Acid Solution. *Jpn. J. Appl. Phys.* **1998**, *37*, L1340−L1342.
(44) Jessensky, O.; Müller, F.; Gösele, U. Self-organized Formation of Hexagonal Pore Arrays in Anodic Alumina. *Appl. Phys. Lett.* **1998**, *72*, 1173−1175.
(45) French, R. H.; Müllejans, H.; Jones, D. J. Optical Properties of Aluminum Oxide: Determined from Vacuum Ultraviolet and Electron Energy-Loss Spectroscopies. *J. Am. Ceram. Soc.* **1998**, *81*, 2549−2557.
(46) Abràmoff, M. D.; Magalhaes, P. J.; Ram, S. J. Image Processing with ImageJ. *Biophotonics Int.* **2004**, *11*, 36−42.
(47) Surawathanawises, K.; Cheng, X. Nanoporous Anodic Aluminum Oxide with a Long-Range Order and Tunable Cell Sizes by Phosphoric Acid Anodization on Pre-patterned Substrates. *Electrochem. Acta* **2014**, *117*, 498−503.
(48) Law, C. S.; Sylvia, G. M.; Nemati, M.; Yu, J.; Losic, D.; Abell, A. D.; Santos, A. Engineering of Surface Chemistry for Enhanced Sensitivity in Nanoporous Interferometric Sensing Platforms. *ACS Appl. Mater. Interfaces* **2017**, *9*, 8929−8940.
(49) Stępniowski, W. J.; Zasada, D.; Bojar, Z. First Step of Anodization Influences the Final Nanopore Arrangement in Anodized Alumina. *Surf. Coat. Technol.* **2011**, *206*, 1416−1422.
(50) Li, C.-Y.; Wu, Z.-Q.; Yuan, C.-G.; Wang, K.; Xia, X.-H. Propagation of Concentration Polarization Affecting Ions Transport in Branching Nanochannel Array. *Anal. Chem.* **2015**, *87*, 8194−8202.
(51) Wang, Y.; Santos, A.; Kaur, G.; Evdokiou, A.; Losic, D. Structurally Engineered Anodic Alumina Nanotubes as Nano-Carriers for Delivery of Anticancer Therapeutics. *Biomaterials* **2014**, *35*, 5517−5526.
(52) Nielsch, K.; Choi, J.; Schwirn, K.; Wehrspohn, R. B.; Gösele, U. Self-Ordering Regimes of Porous Alumina: The 10% Porosity Rule. *Nano Lett.* **2002**, *2*, 677−680.

https://doi.org/10.1021/acsami.2c02369
ACS Appl. Mater. Interfaces XXXX, XXX, XXX−XXX

(53) Kumeria, T.; Santos, A.; Rahman, M. M.; Ferré-Borrull, J.; Marsal, L. F.; Losic, D. Advanced Structural Engineering of Nanoporous Photonic Structures: Tailoring Nanopore Architecture to Enhance Sensing Properties. *ACS Photonics* **2014**, *1*, 1298−1306.
(54) Buijnsters, J. G.; Zhong, R.; Tsyntsaru, N.; Celis, J.-P. Surface Wettability of Macroporous Anodized Aluminum Oxide. *ACS Appl. Mater. Interfaces* **2013**, *5*, 3224−3233.
(55) Piwoński, I.; Grobelny, J.; Cichomski, M.; Celichowski, G.; Rogowski, J. Investigation of 3-mercaptopropyltrimethoxysilane Self-assembled Monolayers on Au (111) Surface. *Appl. Surf. Sci.* **2005**, *242*, 147−153.

https://doi.org/10.1021/acsami.2c02369
ACS Appl. Mater. Interfaces XXXX, XXX, XXX−XXX